LAWRENCE
LIVERMORE
NATIONAL
LABORATORY

UCRL-TR-201817

Methods for Calculating a Simplified Hydrologic Source Term for Frenchman Flat Sensitivity Studies of Radionuclide Transport Away from Underground Nuclear Tests

A. F. B. Tompson, M. Zavarin,
C. J. Bruton, and G. A. Pawloski

January 5, 2004

DISCLAIMER

Work performed under the auspices of the U. S. Department of Energy by the University of California, Lawrence Livermore National Laboratory under contract W-7405-ENG-48.

Contents

Methods for Calculating a Simplified Hydrologic Source Term for Frenchman Flat Sensitivity Studies of Radionuclide Transport Away from Underground Nuclear Tests

1. Introduction

The purpose of this report is to provide an approach for the development of a simplified unclassified hydrologic source term (HST) for the ten underground nuclear tests conducted in the Frenchman Flat Corrective Action Unit (CAU) at the Nevada Test Site (NTS). It is being prepared in an analytic form for incorporation into a GOLDSIM (Golder Associates, 2000) model of radionuclide release and migration in the Frenchman Flat CAU. This model will be used to explore, in an approximate and probabilistic fashion, sensitivities of the 1,000-year radionuclide contaminant boundary (FFACO, 1996; 2000) to hydrologic and other related parameters.

The total inventory (or quantity) of radionuclides associated with each individual test, regardless of its form and distribution, is referred to as the radiologic source term (RST) of that test. The subsequent release of these radionuclides over time into groundwater is referred to as the hydrologic source term (HST) of that test (Tompson, et al., 2002). The basic elements of the simplified hydrologic source term model include

- Estimation of the volumes of geologic material physically affected by the tests.
- Identification, quantification, and distribution of the radionuclides of importance.
- Development of simplified release and retardation models for these radionuclides in groundwater.

The simplifications used in the current HST model are based upon more fundamental analyses that are too complicated for use in a GOLDSIM sensitivity study. These analyses are based upon complex, three-dimensional flow and reactive transport simulations summarized in the original CAMBRIC hydrologic source term model (Tompson et al., 1999), unclassified improvements of this model discussed in Pawloski et al. (2000), as well as more recent studies that are part of an ongoing model of the HST at the CHESHIRE test in Pahute Mesa (Pawloski et al., 2001).

2. Test Configurations, Radionuclide Inventories and Their Distribution

The ten underground nuclear tests associated with the Frenchman Flat CAU (conducted in Areas 5 and 11 at the NTS) are summarized in Table 2.1. They were located in alluvium, with the exception of PIN STRIPE, which was in a chemically similar volcanic tuff formation. Following Underground Test Area (UGTA) programmatic decisions, we assume that the cavity, melt glass, and exchange volume of each test—where radionuclide inventories are concentrated—lie in the saturated zone, beneath the static water table.

2.1 Parametric Test Information

The volumes of geologic material affected by a test explosion must be determined in order to estimate the initial locations and distribution of radionuclides. Since the appropriate parametric data used to describe these volumes are determined from yield, the tests have been arranged into three **groups** (A, B, or C) in which the yields (and, thus, the volumes) are equal, or nearly so, as indicated in Table 2.1. Note that in most cases the announced yield is a range and that the upper limit of this range was used to evaluate various yield-dependent parameters and identify the A, B, and C groups.

Table 2.1. Underground nuclear tests conducted in the Frenchman Flat CAU, in order of announced yield range, and related parametric information. Row shading demarcates 3 groups of tests with unique melt glass (V_g) and exchange volume magnitudes (V_e).

Group	Name[a]	Test date[a] (m–d–y)	Ann. yield range (kt)[a]	Est. depth to working point, h (m)[b]	Est. cavity radius, R_c (m)[c]	Est. melt glass mass, M_g (kg)[d]	Est. bulk melt glass volume, V_g (m^3)[e]	Est. bulk exchange volume V_e (m^3)[f,g]
A	CAMBRIC	5-14-1965	0.75	295	11[h]	5.25×105	263	1.88×104
B	DERRINGER	9-12-1966	7.8	255	29	5.46×10^6	2,730	3.45×10^5
C	WISHBONE	2-18-1965	<20	175	43	$1.4. \times 10^7$	7,000	1.12×10^6
	DILUTED WATERS	6-16-1965	<20	193	42	$1.4. \times 10^7$	7,000	1.05×10^6
	MILK SHAKE	3-25-1968	<20	265	39	$1.4. \times 10^7$	7,000	8.39×10^5
	PIN STRIPE	4-25-1966	<20	296	38	$1.4. \times 10^7$	7,000	7.76×10^5
	NEW POINT	12-13-1966	<20	239	40	$1.4. \times 10^7$	7,000	9.05×10^5
	DIANA MOON	8-27-1968	<20	242	40	$1.4. \times 10^7$	7,000	9.05×10^5
	MINUTE STEAK	9-12-1969	<20	265	39	$1.4. \times 10^7$	7,000	8.39×10^5
	DIAGONAL LINE	11-24-1971	<20	264	39	$1.4. \times 10^7$	7,000	8.39×10^5

[a] USDOE (2000).
[b] USDOE (1999).
[c] Based upon maximum yield and Equation 2.1 with $r_b = 2.1$ g/cm^3.
[d] Based upon maximum yield and 700,000 kg-glass per kiloton of yield.
[e] Based upon maximum yield and Equation 2.2 with $r_g = 2.5$ g/cm^3 and $f_g = 0.2$.
[f] Based upon a sphere of radius 1.5 R_c (Section 2.1).
[g] Mean cavity radius for a group 'C' test, 40 m, leads to mean value of $V_e = 9.05 \times 10^5$ m^3.
[h] Measured value (Hoffman et al., 1977).

The cavity radius (R_c) for each test may be estimated from (Pawloski, 1999)

$$R_c \approx \frac{70.2\, y^{1/3}}{\left(\rho_b h\right)^{1/4}} \tag{2.1}$$

where y is the test yield (in kt), h is the working point depth (in m), and ρ_b is the bulk density (Mg/m^3 or g/cm^3) of the overlying materials—assumed here to be approximately 2.1 g/cm^3 for all Frenchman Flat tests. Estimates of R_c for each test in the Frenchman Flat CAU are provided in Table 2.1. When the yield is shown to be a range, the maximum value was used. The value of R_c shown for the CAMBRIC test was measured (Hoffman et al., 1977).

The melt glass is known to be a heterogeneous brecciated mixture of vesicular and massive glass in which the heavier radionuclides are preferentially sequestered. The amount of melt glass (M_g) produced in a test is related to the yield of the test. Approximately 700 metric tons (700,000 kg) of glass are typically produced per kiloton of test yield (Pawloski, 1999). The bulk volume (V_g) of the melt glass zone can thus be estimated from

$$V_g = \frac{M_g}{\rho_g(1-\phi_g)} = \frac{700{,}000\ \text{(kg/kt)} \cdot y}{\rho_g(1-\phi_g)}. \tag{2.2}$$

The bulk volume is a function of the interstitial porosity (ϕ) and intrinsic density (ρ) of the glass. Using an intrinsic glass density of ρ_g = 2.5 g/cm^3 (i.e., 2,500 kg/m^3), an assumed glass porosity of ϕ_g = 0.2, and the upper bound of the yield estimates shown in Table 2.1, the estimated amount of melt glass and the bulk glass volume associated with each test can be computed from (2.2) and is shown in Table 2.1.

The volume of rubblized and contaminated rock typically extends beyond the cavity to points ranging between 1.3 to 2 R_c away from the working point (Borg, 1976). Pawloski (1999) recommends use of a value of 1.5 R_c to estimate the size of the "damaged zone." For our current purpose, this zone will be considered equivalent to the "exchange volume" in which radionuclides are initially confined, and will be approximated as a sphere centered on the working point with a radius equal to 1.5 R_c. Estimates of its volume (V_e) using this relationship and the values of R_c shown in Table 2.1 are also shown in Table 2.1.

2.2 Radiologic Source Term Inventory and Distribution Information

Although the radiologic inventory (or radiologic source term, RST) for each underground test in Frenchman Flat is classified, the total inventory for all underground tests in Frenchman Flat has recently been declassified and is reported in Bowen et al. (2001).

As a means to identify the most important radionuclides for this study, we considered those listed in the Bowen et al. (2001) tabulations as the most relevant candidates (Table 2.2).

These should not be considered an exhaustive list of all possible test-related radionuclides, but, rather, those with sufficiently long half-lives and abundance to be of regulatory concern over the next 1,000 years, as discussed by Wild et al. (1998) and Bowen et al. (2001). If desired, this list could be shortened in a systematic way using a procedure like that employed in Pawloski et al. (2002) and summarized by Daniels et al. (2001).

An average inventory for each radionuclide in Table 2.2 was found by dividing the total Frenchman Flat inventory reported in Bowen et al. (2001) by 10, as shown in Table 2.2. These values are decay corrected to September 23, 1992. As in Pawloski et al. (2002), the average inventory data may be applied as an unclassified RST at each testing site in Frenchman Flat, as long as it is understood that they do not represent the inventory of any specific test in Frenchman Flat. In the specific case of the CAMBRIC test, unclassified inventory estimates for some radionuclides (e.g., ^{3}H, ^{85}Kr, ^{90}Sr, ^{99}Tc, ^{137}Cs, ^{238}U, and ^{239}Pu) have been developed via other means (see Tompson et al., 1999) and may, instead, be considered as components of an unclassified RST at CAMBRIC.

The distribution of radionuclides between the melt glass and exchange volume can be estimated from the thermodynamic properties of the elements and diagnostic test data. Recommended values in Table 2.2 are derived from IAEA, (1998a) and include separate "water" and "gas" phase categories. In the current work, inventory fractions assigned to the "rubble," "water," and "gas" phases will be combined and assumed to be uniformly distributed within the groundwater of the exchange volume[1]. The combined amount of radionuclides assigned to the groundwater may be further subdivided into dissolved and sorbed components, to the extent that sorbing minerals exist in the exchange volume and to the extent that the particular radionuclides partake in sorption reactions.

It should be noted that the reported inventories of ^{40}K, ^{232}Th, ^{234}U, ^{235}U, and ^{238}U include estimates of their natural (non test-related) abundance that was incorporated in melt glass. With the exception of ^{40}K, the amount of these radionuclides that is either natural or test-related in origin has not been determined (although it has in the case of the unclassified Pahute Mesa inventory, Smith, 2001). Because ^{40}K is entirely of natural origin, it will not be considered further as a component of the source term.

1 This differs slightly from the initial radionuclide distribution method used in Tompson et al. (1999) but does not result in a significant change in radionuclide breakthrough.

Table 2.2. Average molar inventories (N) of 44 candidate radionuclides for the 10 underground tests in Frenchman Flat, corrected to September 23, 1992. With the exception of ^{150,152}Gd, these were derived from the data in Bowen et al. (2001). Their initial distribution among the melt glass, rubble (exchange volume), gas, and water phases is shown. Isotopes in unshaded rows decay to stable nonradioactive daughter products and have no decay-related parents. Isotopes in shaded rows are part of important decay chains (see text). Since ^{40}K is entirely of natural origin, it is not considered a member of the RST (see footnote d). $^{150, 152}$Gd were identified as additional and potentially important members of the RST (see footnotes g, i) even though they were not reported in Bowen et al. (2001).

RN	Half life (y)[a]	Average radiologic inventory, N (mol)	Distribution of total inventory (%)			
			Melt glass	Rubble	Gas	Water
^{3}H	12.3	0.601	0	0	2	98
^{14}C	5.73×10^{3}	0.106	0	10	80	10
^{26}Al[b]	7.30×10^{5}	1.40×10^{-3}	95	5	0	0
^{36}Cl	3.01×10^{5}	0.750	50	40	0	10
^{39}Ar[c]	269	4.64×10^{-4}	0	10	80	10
^{40}K[d]	1.28×10^{9}	5.86×10^{2}	100[d]	0[d]	0	0
^{41}Ca	1.03×10^{5}	1.88	70	30	0	0
^{59}Ni	7.6×10^{4}	0.0348	95	5	0	0
^{63}Ni	100	4.70×10^{-3}	95	5	0	0
^{85}Kr	10.7	3.87×10^{-4}	0	10	80	10
^{90}Sr	29.1	0.0151	40	60	0	0
^{93}Zr	1.50×10^{6}	0.0470	95	5	0	0
^{93m}Nb	16.1	0.0	95	5	0	0
^{94}Nb[e]	2×10^{4}	3.90×10^{-3}	95	5	0	0
^{99}Tc	2.13×10^{5}	0.0696	80	20	0	0
^{107}Pd	6.5×10^{6}	0.0355	70	30	0	0
^{113m}Cd	14.1	1.18×10^{-5}	70	30	0	0
^{121m}Sn	55	2.53×10^{-4}	60	40	0	0
^{126}Sn	1×10^{5}	5.73×10^{-3}	70	30	0	0
^{129}I	1.57×10^{7}	0.0199	50	40	0	10
^{135}Cs	2.3×10^{6}	0.0876	20	80	0	0
^{137}Cs[f]	30.2	0.0424	20	80	0	0
^{151}Sm	90	7.42×10^{-3}	95	5	0	0
^{150}Gd[g,h]	1.8×10^{6}	1.73×10^{-12}	95	5	0	0
^{150}Eu[h]	36	9.93×10^{-8}	95	5	0	0
^{152}Gd[h,i]	1.1×10^{14}	0	[i]	[i]	[i]	[i]
^{152}Eu	13.5	2.87×10^{-3}	95	5	0	0
^{154}Eu	8.59	6.30×10^{-4}	95	5	0	0
^{166m}Ho[h]	1.2×10^{3}	6.80×10^{-4}	95	5	0	0
^{232}Th[j]	1.4×10^{10}	4.68×10^{2}	95	5	0	0
^{232}U[j]	70	2.01×10^{-7}	90	10	0	0
^{233}U	1.59×10^{5}	5.94×10^{-5}	90	10	0	0
^{234}U[k]	2.46×10^{5}	0.0297	90	10	0	0

Table 2.2 (continued).

RN	Half life (y)[a]	Average radiologic inventory, N (mol)	Distribution of total inventory (%)			
			Melt glass	Rubble	Gas	Water
^{235}U[k]	7.04×10^{8}	1.69	90	10	0	0
^{236}U	2.34×10^{7}	1.96×10^{-3}	90	10	0	0
^{238}U[k]	4.47×10^{9}	11.9	90	10	0	0
^{237}Np	2.14×10^{6}	8.25×10^{-3}	95	5	0	0
^{238}Pu[k]	87.7	7.93×10^{-3}	95	5	0	0
^{239}Pu[l]	2.41×10^{4}	9.54	95	5	0	0
^{240}Pu[l]	6.56×10^{3}	0.640	95	5	0	0
^{241}Pu[l]	14.4	0.0178	95	5	0	0
^{242}Pu[l]	3.75×10^{5}	3.02×10^{-3}	95	5	0	0
^{241}Am[m]	433	0.0608	95	5	0	0
^{243}Am[m]	7.37×10^{3}	0.0	95	5	0	0
^{244}Cm[m]	18.1	0.0	95	5	0	0

[a] Half-lives taken from Walker et al. (1989). In our 1,000-yr HST calculations, we consider a radionuclide to be "effectively stable" if its half-life is > 6580 years. The half life and decay rate are related by $l = \ln(2)/t_{1/2}$.

[b] Distribution data for ^{26}Al were not listed in IAEA (1998a). An analysis of its boiling point indicates that it is likely a refractory isotope and is analogous in its distribution to the rare-earths and uranium.

[c] Distribution data for ^{39}Ar were not listed in IAEA (1998a) and were assumed to be equal to ^{85}Kr.

[d] The reported inventories of ^{40}K, ^{232}Th, ^{234}U. ^{235}U, and ^{238}U include estimates of their natural (non test-related) abundance that was incorporated in melt glass. With the exception of ^{40}K, the amount of these radionuclides that is either natural or test-related in origin has not been determined. Because ^{40}K is entirely of natural origin, it will not be considered further as a component of the source term.

[e] Distribution data for ^{94}Nb were not listed in IAEA (1998a) and were assumed to be equal to ^{93}Nb.

[f] Distribution data for ^{137}Cs were assumed equivalent to those for ^{135}Cs to simplify model calculations.

[g] Because of its alpha emission, ^{150}Gd ($t_{1/2} = 1.8 \times 10^{6}$ y) was identified as a potentially important member of the RST, even though it was not reported in Bowen et al. (2001). ^{150}Gd is created from decay of ^{150m}Eu ($t_{1/2} = 12.6$ h), which is originally generated as 30% of the total $^{150+150m}Eu$ production (D. K. Smith, personal communication). The reported value of ^{150}Eu represents the longer-lived 70% fraction ($t_{1/2} = 36$ y). The 30% ^{150m}Eu fraction was excluded from the Bowen et al. (2001) report because of its short half-life, even though it was included in the unclassified Pahute Mesa inventory reported by Smith (2001).

[h] Distribution data for ^{150}Gd and ^{166m}Ho were not listed in IAEA (1998a) and were assumed to be equal to ^{152}Eu.

[l] ^{152}Gd ($t_{1/2} = 1.1 \times 10^{14}$ y) was identified as a potentially important daughter product of ^{152}Eu. Since it has no initial abundance, its distributional characteristics were assumed to parallel those of its parent, ^{152}Eu.

[j] Distribution data for ^{232}Th were not listed in IAEA (1998a) and were assumed to be equal to ^{229}Th.

[k] Distribution data for these U isotopes were not listed in IAEA (1998a) and were assumed to be equal to those for ^{233}U and ^{236}U.

[l] Pu and Am distributions were more conservatively estimated at 5% in rubble instead of 2%.

[m] Distribution data for ^{243}Am and ^{244}Cm were not listed in IAEA (1998a) and were assumed to be equal to ^{241}Am.

2.3 Radioactive Decay

Radioactive decay and ingrowth must be considered in order to (a) identify whether any important daughter products need to be addressed as members of the RST, and (b) determine whether coupled ingrowth and decay affect the relative abundance of any RST radionuclides.

By definition, all 44 radionuclides in the RST of Table 2.2 will undergo some form of radioactive decay. A total of 20 radionuclides with low to intermediate atomic numbers (<80) will decay into stable, nonradioactive daughter products and have no parent radionuclides in the RST. An additional four members of the RST decay into short-lived radioactive daughter

products, which, in turn, decay into stable granddaughters. These short-lived intermediaries will exist in secular equilibrium (Friedlander et al., 1981), and will not be considered because their abundance can independently be computed in terms of their parents' abundance. Nineteen of the heavier radionuclides in the RST are members of nine additional coupled decay chains that need to be considered more carefully in terms of items (a) and (b) above. Their consideration has led to the inclusion of an additional radionuclide that was identified as a potentially important daughter product, albeit previously unreported. The 13 decay chains are discussed in Appendix A.

Based upon discussion in Pawloski et al. (2002) and Appendix A, we recommend for the 1,000-year simplified source term analysis that:

- The decay of RST radionuclides with stable, nonradioactive daughter products and no parent radionuclides be addressed in a post-processing step, after transport calculations have been finished (Tompson et al., 1999). These radionuclides are indicated by the unshaded rows of Table 2.2.
- Radionuclides with half-lives greater than a critical value of 6,580 years be considered "effectively" stable[2]. This means that the coupling between decay and ingrowth in the 13 decay chains discussed in Appendix A can be limited to the 10 radionuclides that appear in the following four abridged chains:

  ^{152}Eu (28%) $\rightarrow$ ^{152}Gd (effectively stable)

  $^{241}Pu \rightarrow {}^{241}Am \rightarrow {}^{237}Np$ (effectively stable)

  $^{238}Pu \rightarrow {}^{234}U$ (effectively stable)

  $^{244}Cm \rightarrow {}^{240}Pu \rightarrow {}^{236}U$ (effectively stable)

- The parent nuclides in these chains, above the effectively stable daughters, are listed in the darkly shaded rows of Table 2.2. Their decay must be treated in a real-time fashion in order to determine the ingrowth of the daughter radionuclides. Notably, only one derivative radionuclide arises at the end of this process. ^{152}Gd, in bold, is produced from the decay of ^{152}Eu along a 28% branch ratio, and has no initial abundance. It represents an additional—or derivative—member of the RST that was not listed in Bowen et al. (2001). The remaining 72% of ^{152}Eu decays to a stable, nonradioactive daughter product.
- The decay of all remaining radionuclides in the lightly shaded rows of Table 2.2 can also be addressed in a post-processing step, after transport calculations have been finished (e.g., Tompson et al., 1999). This is because (a) they may be considered effectively stable or (b) we are ignoring intermediary daughter products because they are short-lived.

[2] The original inventory of a radionuclide that meets this criterion will be reduced by less than 10% over a 1,000-year period. Although decay of such a radionuclide will not contribute to substantial ingrowth of daughter products over this period, the daughters will exist in small amounts, and may need to be considered further.

3. Radionuclide Release from the Exchange Volume and Melt Glass

3.1 Initial State

We assume an initial state in which the respective fractions of the RST (Table 2.2) are uniformly distributed within the melt glass and exchange volume of each test. This comprises the initially contaminated region for each test. In this work, inventory fractions assigned to the "rubble," "gas," and "water" phases are combined and assigned to the exchange volume, where they are distributed among aqueous and sorbed states in alluvium as described below.

3.2 Release Simplifications

The release of radionuclides from the glass and exchange volume will be influenced by groundwater flow and transport processes, geochemical behavior associated with ion exchange and surface complexation onto geologic media, aqueous speciation and precipitation reactions, and dissolution of melt glass. Although these processes can be rather complex (e.g. Tompson et al., 1999), we will assume that they can be simplified to the extent that

- The temperature is fixed at 25°C such that there are no thermally induced flow effects or accelerated dissolution processes produced from residual heat of any test (Maxwell et al., 2000; Pawloski et al., 2001; Tompson et al., 2002).
- Groundwater flow is steady.
- Ion exchange and surface complexation reactions can be described by simple retardation coefficients that are functions of the geologic medium and ambient groundwater chemistry.
- Melt glass dissolution is represented by an approximately constant rate and an unchanging glass porosity of $\phi_g = 0.20$.
- Radionuclide mineral precipitation/dissolution and formation of radionuclide-sorbing minerals in the melt glass or elsewhere is ignored.
- Dissolution of naturally-occurring radionuclides (e.g., ^{232}Th, ^{234}U, ^{235}U, and ^{238}U) from collapsed rubble is not considered, even though their natural abundance in the melt glass is included in the RST total.
- Diffusive mass transport is not considered, despite the fact that low permeability in the melt glass (as generally conceptualized) may limit groundwater advection and increase the relative importance of diffusion as a transport mechanism.
- The near-field alluvium has a porosity of $\phi_g = 0.40$ and a spatially constant mineralogic composition.
- The groundwater pH is fixed at a value of 8.0.

As a result of these assumptions, the mathematics of groundwater flow, chemical reaction, melt glass dissolution, and their collective interaction will become linear and scalable,

permitting, for example, modification of the inventories in Table 2.2 for sensitivity analysis purposes.

The list of radionuclides in Table 2.2 can be recombined into 11 distinct radionuclide **classes** with unique partitioning and sorption characteristics, as shown in Table 3.1. Appendix B describes in detail how these classes and sorption parameters were defined. For the purposes of this table, unit molar inventories were assumed in order to simplify the distribution information shown in the last two columns. Actual distribution information for particular radionuclides can be found by multiplying the total inventory of that radionuclide (such as found in column 3 of Table 2.2) with the fractions listed in the last two columns of Table 3.1).

The sorption information in Table 3.1 is representative of the net effect of all sorbing minerals (smectite, illite, zeolite, calcite, and goethite or hematite) identified by x-ray diffraction in Frenchman Flat alluvium. Individual sorption coefficients were derived for each sorbing mineral and radionuclide pair, as shown in Tables B.3 and B.4 in Appendix B, and recombined into one effective value shown in the "$\mathrm{Log}_{10}\ K_d^i$" columns of Table 3.1. Different effective values of the K_d parameter are provided depending on whether a hematite or goethite form of iron oxide is used to define the Frenchman Flat alluvium mineralogy. Mean, high, and low values of the parameter are included in the table for sensitivity study purposes. Because sorption information for some radionuclides is not available, they are specifically treated as tracer analogs (e.g., ^{26}Al, ^{59}Ni, ^{63}Ni, ^{93}Zr, ^{93m}Nb, ^{94}Nb, ^{107}Pd, ^{113m}Cd, ^{121}Sn, ^{126}Sn, and ^{232}Th) or as analogs to other sorbing radionuclides (e.g., ^{150},^{152}Gd, ^{166m}Ho, and ^{244}Cm).

3.3 Basic Problem Conceptualization

Our basic conceptualization of groundwater flow through the initially contaminated region surrounding a typical saturated zone test is shown in Figure 3.1. In this figure, the exchange volume (which includes the cavity) is shown in yellow, with a bulk volume V_e, while the melt glass is shown just below it (in blue), with a bulk volume V_g. Groundwater flow through these regions is assumed to be steady and is shown to be encapsulated within two curvilinear streamtubes that individually and completely envelop each zone (Tompson et al., 1999). If diffusive or dispersive mass transport across streamtube boundaries is ignored, the streamtubes will contain all radionuclides that migrate away from the initially contaminated region, as shown in the highlighted segments in Figure 3.1 and indicated by radionuclide fluxes J^e and J^g.

Although the total flow rate in each streamtube (Q_e and Q_g) will be constant, the cross-sectional area (A_e and A_g) and Darcy flux (q_e and q_g) along the axis of each streamtube may vary with position, owing to the effects local medium heterogeneity. As shown in the individual panels of Figure 3.1, fundamental contrasts in hydraulic conductivity between the background, undisturbed media (K), exchange (and cavity) volumes (K_e), and melt glass region (K_g) give rise to streamtubes that converge or diverge about the disturbed zone. In a limiting case (bottom image), the melt glass is assumed to have virtually no permeability ($K_g \sim 0$) such that flow is completely diverted around it.

Table 3.1. Simplified inventory, with indicated means and (high, low) ranges of $\log_{10} K_d^i$ for 11 specific classes of radionuclides.[a] Note that K_d^i is an effective value based upon the assumed abundance of all sorbing minerals (Table B.1). Initial moles expressed per mole inventory and based upon partitioning data shown in Table 2.2.

RN class	Component		RN analogs	$\text{Log}_{10}\ K_d^i$ (mL/g)		Initial moles (mol) per mole inventory	
				Goethite alluvium	Hematite alluvium	Melt glass, N_g	Exchange volume, N_e
1	Tracer 1[b]	^{3}H, ^{14}C, ^{36}Cl, ^{39}Ar, ^{85}Kr, ^{99}Tc, ^{129}I[c]	^{26}Al[c], ^{59}Ni[c], ^{63}Ni[c], ^{93}Zr[c], ^{93m}Nb[c], ^{94}Nb[c], ^{107}Pd[c], ^{113m}Cd[c], ^{121}Sn[c], ^{126}Sn[c], ^{232}Th[c]	0	0	0.0	1.0
2	Tracer 2[b]			0	0	1.0	0.0
3	^{41}Ca			2.4 (2.4, 2.4)	2.4 (2.4, 2.4)	0.70	0.30
4	^{90}Sr			2.5 (2.5, 2.4)	2.5 (2.5, 2.4)	0.40	0.60
5	$^{135,137}Cs$			3.0 (3.0, 2.2)	3.0 (3.0, 2.1)	0.20	0.80
6	^{151}Sm			4.6 (5.6,3.5)	4.4 (5.3, 3.4)	0.95	0.05
7a	$^{150,154}Eu$		$^{150,152}Gd$[d,e], ^{166m}Ho[d]	4.2 (5.3, 3.1)	3.9 (4.9, 2.9)	0.95	0.05
7b	^{152}Eu						
7c			^{244}Cm[d]				
8	$^{232,233,234,235,236,238}U$			2.9 (3.8, 2.1)	1.7 (2.6, 0.9)	0.90	0.10
9	^{237}Np			2.3 (3.2, 1.6)	1.5 (2.4, 0.7)	0.95	0.05
10a	$^{239,242}Pu$			3.0 (4.0, 2.0)	2.0 (3.0, 1.0)	0.95	0.05
10b	^{238}Pu						
10c	^{240}Pu						
10d	^{241}Pu						
11a	^{243}Am			4.3 (5.2, 3.5)	4.2 (5.1, 3.3)	0.95	0.05
11b	^{241}Am						

[a] Note that the familiar "retardation factor" can be written as $R_i = 1 + \rho_b K_d^i / \phi$ where ϕ =0.4 and ρ_b = 2.1 g/cm^3 are the porosity and bulk density of the alluvium.

[b] The behavior of non-sorbing radionuclides is described by defining two tracers of unit mole inventory in the melt glass and exchange volume, respectively. The behavior of each non-sorbing radionuclide can be determined by proportionally combining results for each tracer and then accounting for decay.

[c] ^{26}Al, ^{59}Ni, ^{63}Ni, ^{93}Zr, ^{93m}Nb, ^{94}Nb, ^{107}Pd, ^{113m}Cd, ^{121}Sn, ^{126}Sn, and ^{232}Th are described as tracers because their reactive transport behavior has not been determined, even though many (e.g., ^{113m}Cd and ^{232}Th) are expected to be highly sorbing.

[d] $^{150,152}Gd$, ^{166m}Ho, and ^{244}Cm sorption behavior is assumed to be equivalent to that of Eu.

[e] There is no initial abundance of ^{152}Gd; it is only produced by ingrowth.

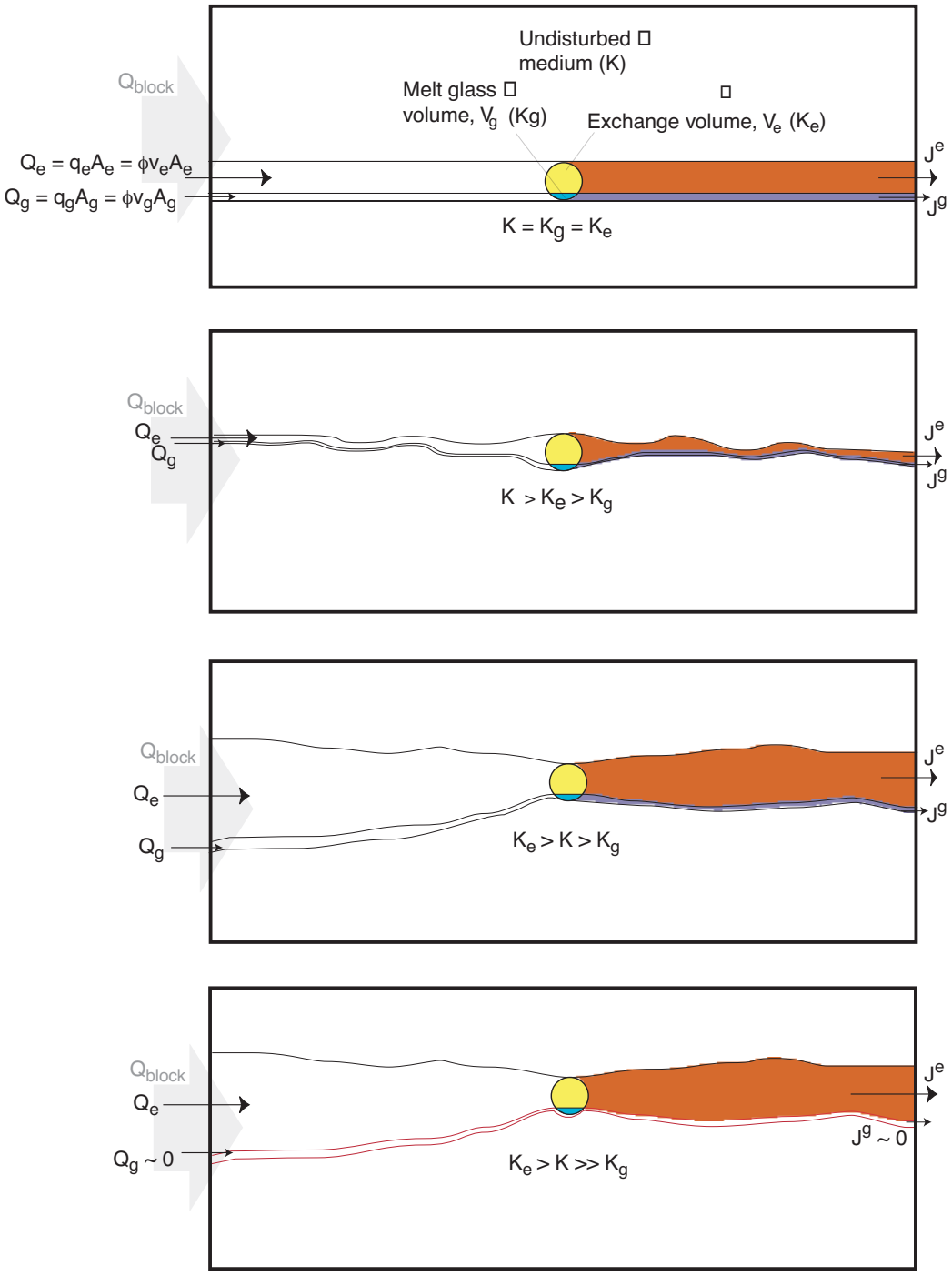

Figure 3.1. Basic conceptualization of steady ambient groundwater flow through the exchange (and cavity) volumes and melt glass region of a typical saturated zone test. Flow is shown to occur through two distinct streamtubes with variable cross sectional areas (A_e and A_g) and Darcy fluxes (q_e and q_g), yet fixed total flow rates (Q_e and Q_g). Radionuclide fluxes (J^e and J^g) are constrained to streamtube volumes. Contrasts in hydraulic conductivity give rise to streamtubes that converge or diverge about the disturbed zone. In the bottom figure, melt glass is assumed to have little or no permeability around which flow is diverted, minimizing radionuclide releases. Larger-scale fluxes (Q_{block}) may pertain to grid-block fluxes calculated in a CAU-scale model.

Flows in the streamtubes should be distinguished from the larger-scale flows through the bounding block of each image (Q_{block}) which may pertain to quantities calculated in a larger-scale (e.g., CAU) model. Because of local heterogeneity, determining one of these flow rates from the other (via scaling arguments, for example) should be carefully considered. Moreover, radionuclide concentrations in each streamtube (and their corresponding fluxes) must be properly calculated and understood before they are scaled and re-incorporated into any such larger-scale groundwater flow and transport model.

In the current simplified model, radionuclide migration within each curvilinear streamtube is conceptualized in a one-dimensional sense in terms of cross-sectionally averaged concentrations and flow rates. Under this assumption, the transport equation for radionuclide *i* in either streamtube takes the form

$$\phi \frac{\partial c_i}{\partial t} + \phi \frac{|\mathbf{v}|}{R_i} \frac{\partial c_i}{\partial s} - \phi \frac{|\mathbf{v}|}{R_i} \frac{\partial}{\partial s}\left(\frac{D}{|\mathbf{v}|} \frac{\partial c_i}{\partial s} \right) = \upsilon_f r_g \quad , \tag{3.1a}$$

where *s* is the spatial coordinate along the streamtube and an appropriate representation of the gradient operators in a curvilinear coordinate system has been used (e.g., Gelhar and Collins, 1971).

In this equation, $|\mathbf{v}|$ is the seepage velocity (m/y) along the streamtube axis, $|\mathbf{q}| = \phi|\mathbf{v}|$ is the corresponding Darcy flux magnitude (m/y), $c_i(s,t)$ is the **aqueous** concentration of radionuclide i (mol/m^3-fluid) in groundwater, and $D = \alpha_L|\mathbf{v}| + D_m$ is the local longitudinal coefficient of hydrodynamic dispersion. Here, α_L is the longitudinal (macro) dispersivity and D_m is an effective molecular diffusivity of the radionuclide. The corresponding **sorbed** concentration (mol-sorbed/m^3-fluid) is denoted by $c_i^s(s,t)$. The quantity R_i is a local retardation factor (dimensionless) associated with radionuclide *i* in alluvium, which can be related to an effective distribution coefficient K_d^i (mL/g) for radionuclide *i* in alluvium using $R_i = 1 + \rho_b K_d^i / \phi$. The quantity $\upsilon_f r_g$ represents the rate of radionuclide release (mol/m^3-y) in the melt glass, as defined in Appendix A, and takes on a zero value elsewhere.

In cases where $D_m << \alpha_L|\mathbf{v}|$, Equation 3.1a can be reexpressed in terms of the constant streamline flux, *Q*, as

$$\frac{\partial c_i}{\partial t} + \frac{Q}{A\phi R_i} \cdot \frac{\partial c_i}{\partial s} - \frac{Q\alpha_L}{A\phi R_i} \cdot \frac{\partial^2 c_i}{\partial s^2} = \frac{\upsilon_f r_g}{A\phi} \tag{3.1b}$$

where $Q = A|\mathbf{q}| = A\phi|\mathbf{v}|$ and A is the cross-sectional area of the streamtube and α_L is assumed constant.

To further simplify this conceptualization, we will assume that the exchange volume and melt glass regions of each test occupy "cubic-shaped" regions that preserve the volumes V_e and V_g cited in Table 2.1. We will also utilize a more localized perspective of the system, as shown in Figure 3.2. Because of this smaller scale, the cross sectional areas, Darcy fluxes, and groundwater velocities will be assumed constant over the streamtube lengths shown in this figure.

In the following sections, we will separately consider the flux of radionuclides past the control plane from each streamtube under the assumptions listed in Section 3.2.

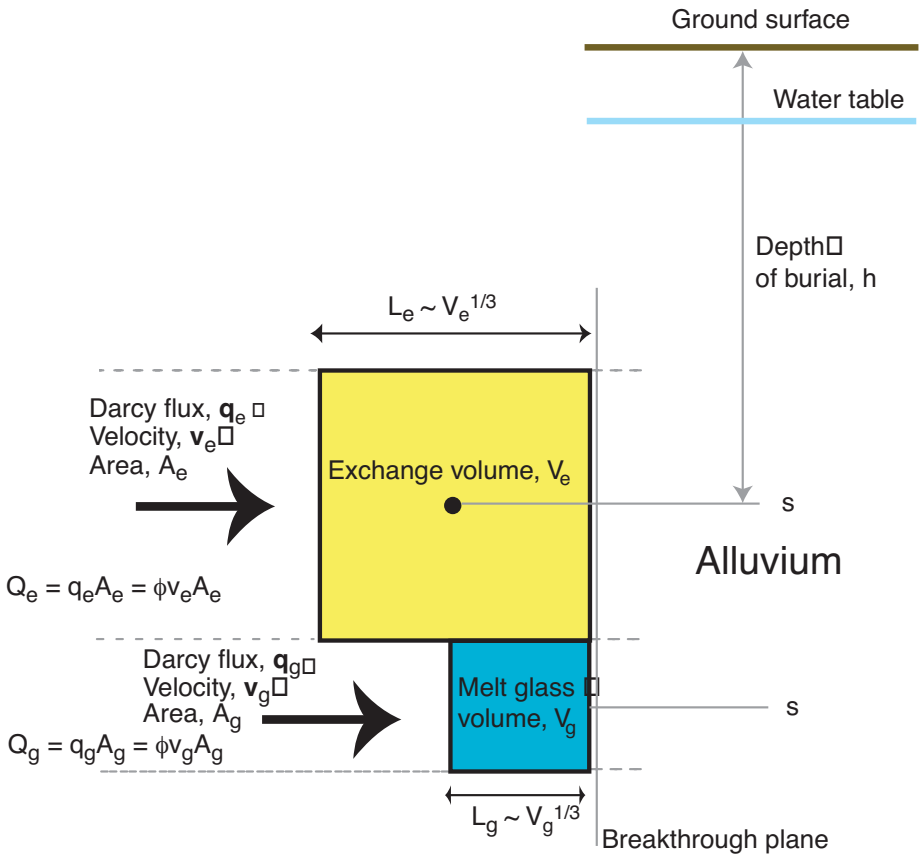

Figure 3.2. Conceptual model of the exchange volume and melt glass volume used for the simplified source term model in this report. The volumes are placed adjacent to a control (or breakthrough) plane across which radionuclide release fluxes are determined. Groundwater flow occurs in two streamtubes, one passing through each volume.

3.4 Release from the Exchange Volume

Radionuclide releases from the exchange volume will be controlled by the groundwater velocity ($\mathbf{v_e}$) or flux (Q_e) through the volume, the initial abundance or concentration of each radionuclide in the volume (c_i^e), and the chemical retardation factor, R_I, (or K_d^i value) associated with each radionuclide. The melt glass dissolution rate v_{fr_g} plays no role in this process because the exchange volume streamtube does not pass through melt glass. Assuming that the radionuclides in the exchange volume are homogeneously distributed initially, their flux (J_i^e) out of the volume (mol/y) past the breakthrough plane shown in Figure 3.2, uncorrected for decay, is given by

$$J_i^e(s_b,t) \approx Q_e c_i^e = A_e \phi \cdot |\mathbf{v}_e| c_i^e \qquad \text{for } 0 < t < R_i L_e / |\mathbf{v}_e| \qquad (3.2a)$$

and

$$J_i^e(s_b,t) \approx 0 \qquad \text{for } t > R_i L_e / |\mathbf{v}_e| \qquad (3.2b)$$

where c_i^e is the initial **aqueous** concentration within the volume, $\mathbf{v_e}$ is the groundwater velocity at the control plane location (s_b), L_e and L_g are the lengths of the exchange and melt glass volumes intersected by the streamtubes, and A_e is the cross-sectional breakthrough area (m^2) of the exchange volume streamtube at the control plane location. Here, we approximate the magnitude of A_e by the 2/3 power of V_e, and the magnitudes of L_e and L_g by the 1/3 power of V_e and V_g, respectively (see Figure 3.2).

The initial **aqueous** concentration in the exchange volume can be determined from

$$c_i^e\left(\mathbf{x} \in \text{exchange volume}, t = 0\right) = \frac{N_e^i}{\phi V_e} \cdot \frac{1}{R_i} \qquad (3.3a)$$

where N_e^i is the number of moles assigned to the exchange volume for radionuclide *i*, and R_i is based upon the relevant sorption data (Table 3.1). Because of sorption, the corresponding initial **sorbed** concentration will be

$$c_i^{s,e}\left(\mathbf{x} \in \text{exchange volume}, t = 0\right) = \frac{N_e^i}{\phi V_e} \cdot \frac{R_i - 1}{R_i} \quad . \qquad (3.3b)$$

Table 3.2 lists the initial exchange volume aqueous concentrations (mol/m^3) **per mole of inventory** for the 11 **classes** of radionuclides (Table 3.1) that should be applied to each of the three test **groups** (Table 2.1), as based upon the mean values for hematite alluvium[3]. Notice that for a fixed molar inventory N_e^i, higher values of R_i lead to smaller, but more long-lived flux rates out of the exchange volume.

[3] These values should be scaled to match the specified inventory, whether it is derived from column 3 of Table 2.2 or elsewhere.

Table 3.2. Initial aqueous concentrations (mol/m^3-fluid)[a] in the exchange volume per mole of inventory[b] for the 11 radionuclide classes and the 3 test groups using Eq. (3.3a). Results based upon mean K_d for hematite alluvium (Table 3.1), partitioning data (Table 2.2), and mean exchange volume magnitude, V_e, for test group C (Table 2.1). Porosity value, ϕ, assumed to be 0.40.

RN class	Mean retardation factor[c], R	Initial aqueous concentration (mol/m^3-fluid)[a] per mole of inventory		
		Test group		
		A	B	C
1	1	1.33×10^{-4}	7.25×10^{-6}	2.76×10^{-6}
2	1	0	0	0
3	1,320	3.02×10^{-8}	1.65×10^{-9}	6.28×10^{-10}
4	1,661	4.80×10^{-8}	2.62×10^{-9}	9.98×10^{-10}
5	5,251	2.03×10^{-8}	1.10×10^{-9}	4.21×10^{-10}
6	131,875	5.04×10^{-11}	2.75×10^{-12}	1.05×10^{-12}
7a, 7b, 7c	41,703	1.59×10^{-10}	8.69×10^{-12}	3.31×10^{-12}
8	264	5.04×10^{-8}	2.74×10^{-9}	1.05×10^{-9}
9	167	3.98×10^{-8}	2.17×10^{-9}	8.27×10^{-10}
10a, 10b, 10c, 10d	526	1.26×10^{-10}	6.89×10^{-10}	2.63×10^{-10}
11a, 11b	104,752	6.35×10^{-11}	3.46×10^{-12}	1.32×10^{-12}

[a] Division of concentrations expressed in mol/m^3 by 1,000 yields concentrations in units of mol/L-fluid.
[b] The average Frenchman Flat inventory in moles for each radionuclide in the RST is given in Table 2.2.
[c] The retardation factor is written as $R_i = 1 + \rho_b K_d^i / \phi$ where ϕ =0.4 and ρ_b = 2.1 g/cm^3 are the porosity and bulk density of the alluvium. Mean value derived from mean K_d value.

The effects of longitudinal dispersion (D) were **excluded** in (3.2) because of the close proximity of the control plane to the exchange volume. If, for example, the control plane is located a distance s_c away from the working point along the streamtube—instead of s_b—and the exchange volume (molar) inventory (N_e) can assumed to be concentrated at the working point of the test, then

$$J_i^e(s_c,t) \approx Q_e \cdot \frac{\left(N_e/\phi A_e\right)}{2\sqrt{\pi D_i^* t}} \exp\left\{\frac{-\left(s_c - V_i^* t\right)^2}{4D_i^* t}\right\} \quad \text{for} \quad t > 0 \qquad (3.4a)$$

where $V_i^* = Q_e / A_e \phi R_i$ and $D_i^* = Q_e \alpha_L / A_e \phi R_i$ are assumed to be approximately constant (Carslaw and Jaeger, 1989) and $\mathbf{v_e}$ and A_e are evaluated at the control plane location.

Alternatively, (3.4a) can be rewritten as

$$J_i^e(s_c,t) \approx |\mathbf{v}_e| \cdot \frac{N_e}{2\sqrt{\pi |\mathbf{v}_e| \alpha_L t / R_i}} \exp\left\{ \frac{-\left(s_c - |\mathbf{v}_e| t / R_i\right)^2}{4 |\mathbf{v}_e| \alpha_L t / R_i} \right\} \quad \text{for} \quad t > 0 \quad . \tag{3.4b}$$

Additional results that reflect the effects of dispersion using a spatially distributed initial inventory (as in Figure 3.2) can also be developed (e.g., Carslaw and Jaeger, 1989, p 54).

3.5 Release from the Melt Glass

The flux of radionuclides in groundwater away from the melt glass region will be controlled by the rate of glass dissolution, r_g and the initial abundance or concentration of each radionuclide in the glass υ_i(Appendix C), as well as the actual size or volume of the melt glass zone.

The **aqueous** concentration of a radionuclide within a fluid parcel passing through a streamtube in the melt glass will increase linearly as a function of the parcel's residence time in the glass zone[4]. Assuming a single "pore volume" of fluid has already moved through the glass, the exit concentration c_i^g (mol/m^3-fluid) of radionuclide *i* in a parcel exiting the melt glass zone (or, equivalently, passing by the breakthrough plane in Figure 3.2) can be approximated by

$$c_i^g \approx \frac{L_g}{|\mathbf{v}_g|} \frac{\nu_i r_g}{\phi} \tag{3.5}$$

where L_g is the length of the streamtube (m) lying inside the glass zone (Figure 3.2). This is an analytic result (see Tompson et al., 1999, Appendix 9) that assumes fixed glass porosity (Appendix C) and no retardation effects within the glass. It is also uncorrected for the effects of decay. The flux of this radionuclide (J_i^g) past the breakthrough plane (mol/y) in Figure 3.2 is given by

$$J_i^g(s_b,t) \approx A_g \phi \cdot |\mathbf{v}_g| \cdot c_i^g \tag{3.6}$$

where A_g is the cross-sectional breakthrough area (m^2) of the streamtube passing through the melt glass. Insertion of Equation 3.5 into Equation 3.6 yields, with some generalization,

[4] This assumes, of course, that the melt glass dissolution rate is constant and that silica (dissolved glass) saturation conditions are not reached in the glass (Appendix C). Should this occur, the exit concentration would be directly proportional (via ν_i) to the silica saturation value.

$$J_i^g(s_b,t) \approx V_g \cdot \nu_i r_g \tag{3.7}$$

where V_g is the bulk volume of the melt glass zone (e.g., Table 2.1). This result indicates that the radionuclide flux derived from melt glass dissolution will be steady for as long as the dissolution rate and bulk glass volume can be assumed constant**,** and that it will **not depend** on the groundwater velocity, even though the concentration at the breakthrough plane will.

Substitution of the simplified rate expression from Appendix C into Equation 3.7 yields

$$J_i^g(s_b,t) \approx V_g \nu_i \cdot \rho_{gb} A_s^m \cdot k^{\text{mod}} \tag{3.8}$$

where A_s^m is the **specific** reactive surface area of the glass per unit mass (m^2-glass /g-glass) and k^{mod} is the modified glass dissolution rate constant (Appendix C).

The mole fraction of radionuclide *i* in the glass (ν_i) is equal the ratio of N_g^i to the moles of glass, which can be computed from the mass of glass, M_g, and the formula weight for glass, f_g (defined here as one mole of glass = 100 g-glass, or 1000 moles of glass = 100 kg-glass),

$$\nu_i = N_g^i \cdot \frac{f_g}{M_g}. \tag{3.9}$$

Knowing that $\rho_{gb} = M_g / V_g$ means that (3.8) can now be written as

$$J_i^g(s_b,t) \approx f_g N_g^i \cdot A_s^m \cdot k^{\text{mod}}, \tag{3.10}$$

or, alternatively, as

$$J_i^g(s_b,t) \approx \nu_i \cdot V_g \cdot A_s \cdot k^{\text{mod}} \tag{3.11}$$

where V_g is the bulk melt glass volume and A_s is the **specific surface area** (per bulk volume, m^2/m^3) of the glass.

3.6 Loss of the Melt Glass

Both (3.10) and (3.11) may also be written simply as

$$J_i^g(s_b,t) \approx \nu_i \times A \times k^{\text{mod}} \tag{3.12}$$

where A is the total intrinsic glass area (Appendix C). By recalling the definition of ν_i, we see that the flux of dissolved glass emanating from the melt zone is just

$$J^g(s_b,t) \approx A \times k^{\mathrm{mod}} \equiv -\frac{1}{f_g} \cdot \frac{dM_g}{dt} \tag{3.13}$$

and is proportional to the overall rate of melt glass dissolution. Although integration of this expression could be used to estimate the overall lifetime of the glass, it would require a more careful consideration of how A and k^{mod} vary with M_g and in time, and will not be pursued here. Our working assumption remains that the magnitudes A and k^{mod} remain approximately constant and that the volume of glass mass lost over 1,000 years remains small.

4. Simple Examples

4.1 "Tracer 1" Source Term

Let us consider the release of "Tracer 1" from the exchange volume of a "Group C" test (Table 2.1). "Tracer 1" corresponds to "RN Class 1" in Table 3.1. For an initial inventory of one mole, the initial aqueous concentration of Tracer 1 in the exchange volume will be, from Table 3.2,

$$c_1^e \approx 2.76 \times 10^{-6} \text{ mol/m}^3 .$$

The cross sectional area for the exchange volume streamtube as it crosses the breakthrough plane can be estimated as the 2/3 power of V_e for a "Group C" test (Table 2.1, footnote g), e.g.,

$$A_e \sim V_e^{2/3} \approx 9{,}356 \text{ m}^2 .$$

Thus, with $\phi = 0.4$ in the alluvium, we have from (3.2)

$$\mathcal{J}_1^e \approx |\mathbf{v}| \cdot 1.03 \times 10^{-2} \text{ mol/y} \quad \text{for} \quad 0 < t < t_{\max} , \tag{4.1a}$$

$$\mathcal{J}_1^e \approx 0 \text{ mol/y} \quad \text{for} \quad 0 < t < t_{\max} , \tag{4.1b}$$

where $t_{\max} = 97 \text{ (m)} / |\mathbf{v}|$ years and it is assumed that the mean groundwater velocity ($|\mathbf{v}|$) through the exchange volume is expressed in units of m/y.

4.2 Tritium Source Term

If we wanted to specifically consider the release of tritium (^{3}H) from a "Group C" test using the average Frenchman Flat inventory defined in Table 2.2, then (4.1a) can be rescaled to yield

$$\mathcal{J}_{3H}^e = \mathcal{J}_1^e \times 0.601 \approx |\mathbf{v}| \cdot 6.19 \times 10^{-3} \text{ mol/y} \quad \text{for} \quad 0 < t < t_{\max} . \tag{4.1c}$$

This result is based upon the fact that 100% of tritium is partitioned into the exchange volume. In addition, to account for the effects of decay, we may post-multiply these results by $e^{-\lambda_{3H} t}$, where $\lambda_{3H} = \ln 2 / 12.3 \text{ y}^{-1}$.

4.3 "Tracer 2" Source Term

Let us consider the release of "Tracer 2" from the melt glass of a "Group C" test (Table 2.1). "Tracer 2" corresponds to "RN Class 2" in Table 3.1. For the melt glass, the release of Tracer 2 will be defined by (3.10). We will assume nominal values of the glass surface area and modified dissolution constant (Appendix C) of

$$A_s^m \sim 0.0026 \text{ m}^2\text{/g-glass}$$

$$k^{\text{mod}} \cong 5.1 \times 10^{-12} \text{ mol-glass/m}^2\text{-sec}$$

Table 3.1 indicates that $N_g^2 = 1.0$ moles of Tracer 2 are initially in the melt glass of the Group A test. Thus, with $f_g = 100$ g-glass/mol-glass,

$$J_2^g \approx 1.33 \times 10^{-13} \text{ mol/sec} = 4.18 \times 10^{-5} \text{ mol/y} \ . \tag{4.2}$$

4.4 ^{36}Cl Source Term

Consider the release of ^{36}Cl from a "Group C" test. ^{36}Cl behaves as a tracer that is released both from the exchange volume (like "Tracer 1" above) and melt glass (like "Tracer 2" above). According to Table 2.2, the actual molar inventory is 0.750 moles, which is split equally between melt glass and the exchange volume. Thus, its release, not accounting for decay, is determined from a combination of the results in Sections 4.1 and 4.3, i.e.,

$$J_{36Cl} \approx (0.5 \cdot J_1^e + 0.5 \cdot J_2^g) \times 0.75,$$

or

$$J_{36Cl} \approx |\mathbf{v}| \cdot 3.86 \times 10^{-3} + 1.57 \times 10^{-5} \text{ mol/y} \quad \text{for} \quad 0 < t < t_{\max} \ , \tag{4.3a}$$

$$J_{36Cl} \approx 1.57 \times 10^{-5} \text{ mol/y} \quad \text{for} \quad t > t_{\max} \ , \tag{4.3b}$$

where $t_{\max} = 97 \text{ (m)} / |\mathbf{v}|$ years and $|\mathbf{v}|$ is the mean groundwater velocity through the exchange volume, expressed in units of m/y. To account for the effects of decay, we must multiply these results by $e^{-\lambda_{36Cl} t}$, where $\lambda_{36Cl} = \ln (2/3.01 \times 10^5)$ y^{-1} although this modification would not alter the release significantly because ^{36}Cl can be considered "effectively stable" as defined earlier.

4.5 ^{90}Sr Source Term

Let us consider the release of ^{90}Sr from the exchange volume and melt glass of a "Group A" test (Table 2.1). ^{90}Sr corresponds to "RN Class 4" in Table 3.1, so, for the exchange volume, the initial aqueous concentration of ^{90}Sr for a unit molar inventory will be, from Table 3.2,

$$c_4^e \approx 4.81 \times 10^{-8} \text{ mol/m}^3 \ .$$

The cross sectional area for the exchange volume streamtube as it crosses the breakthrough plane can be estimated as the 2/3 power of V_e for a "Group A" test (Table 2.1), e.g.,

$$A_e \sim V_e^{2/3} \approx 707 \text{ m}^2 \ .$$

Thus, with $\phi = 0.4$ in the alluvium, we have from (3.2)

$$J_4^e \approx |\mathbf{v}| \cdot 1.36 \times 10^{-5} \text{ mol/y} \quad \text{for} \quad 0 < t < t_{\max} \ , \tag{4.4a}$$

$$J_4^e \approx 0 \text{ mol/y} \quad \text{for} \quad t > t_{\max} \ , \tag{4.4b}$$

assuming the mean groundwater velocity (v) through the exchange volume is expressed in units of m/y, where $t_{\max} = 44{,}000 \text{ (m)} / |\mathbf{v}|$ years.

For the melt glass, the release of ^{90}Sr will be defined by (3.9). We will assume values of the glass surface area and modified dissolution rate described in Appendix C,

$$A_s^m \sim 0.0026 \text{ m}^2\text{/g-glass}$$

$$k^{\text{mod}} \cong 5.1 \times 10^{-12} \text{ mol-glass/m}^2\text{-sec}$$

Table 3.1 indicates that 40% of the of the ^{90}Sr inventory is initially in the melt glass of the Group A test. Thus, with $f_g = 100$ g-glass/mol-glass, we have, for a unit molar inventory,

$$J_4^g \approx 5.30 \times 10^{-13} \text{ mol/sec} = 1.67 \times 10^{-5} \text{ mol/y} \ . \tag{4.5}$$

Thus, if the actual inventory of ^{90}Sr is defined to be the average Frenchman Flat value of 0.0151 moles, the total release may be expressed as $J_{90Sr} \approx (J_4^e + J_4^g) \times 0.0151$, which can be multiplied by $e^{-\lambda_{90Sr} t}$ to assess the impacts of radioactive decay, where t is in years and λ_{90Sr}.= $\ln(2/29.1) \sim 0.024 \text{ y}^{-1}$.

4.6 ^{237}Np Source Term

As a final example, let us consider the release of ^{237}Np from the exchange volume and melt glass of a "Group B" test (Table 2.1). Since ^{237}Np is a member of an important decay chain (Section 2.3),

$$^{241}\text{Pu} \rightarrow {}^{241}\text{Am} \rightarrow {}^{237}\text{Np (effectively stable)} \ ,$$

its release must be calculated in three separate steps.

4.6.1 Release of the initial ^{237}Np inventory. Here, the release of the initial inventory of ^{237}Np can be calculated from the glass and exchange volumes in the same way that was used in the previous examples. This will provide a flux, $J^1_{237\,Np} \approx (J_9^e + J_9^g) \times N_{237\,Np}$, where J_9^e and J_9^g are the exchange volume and melt glass fluxes per mole of inventory of a "Class 9" radionuclide (Table 3.1) and N_{Np} is the molar inventory of ^{237}Np (e.g., from Table 2.2). Because ^{237}Np may

be considered "effectively stable," as defined earlier, its decay over 1,000 years will not be significant and a decay correction will not be necessary.

4.6.2 Release of ^{237}Np derived from ^{241}Pu decay. In the second step, the release of the initial inventory of ^{241}Pu, a "Class 10" radionuclide must first be calculated. This will provide a flux defined in terms of a glass and exchange volume release, e.g., as above, $J_{241Pu} \approx (J_{10}^{e} + J_{10}^{g}) \times N_{241Pu}$, where J_{10}^{e} and J_{10}^{g} are the exchange volume and melt glass fluxes per mole of inventory of a "Class 10" radionuclide (Table 3.1) and N_{241Pu} is the molar inventory of ^{241}Pu (e.g., from Table 2.2). Because ^{241}Pu has a short half life and is involved in an important decay chain, its flux must be corrected for decay, and this will lead to an ingrowth of ^{237}Np, or more specifically, an ingrowth of the ^{237}Np flux. This will be denoted by J_{Np}^{2} and will be calculated in terms of J_{241Pu} using the Bateman Equations (Friedlander et al., 1981):

$$J_{237\,Np}^{2} \approx \left(\frac{\lambda_{241\,Am}}{\lambda_{241Pu} - \lambda_{241\,Am}} e^{-\lambda_{241Pu} t} + \frac{\lambda_{241Pu}}{\lambda_{241\,Am} - \lambda_{241Pu}} e^{-\lambda_{241\,Am} t} + 1 \right) \cdot J_{241Pu}$$

where the decay rates (λ) of both ^{241}Pu and ^{241}Am appear.

4.6.3 Release of ^{237}Np derived from ^{241}Am decay. In the last step, the release of the initial inventory of ^{241}Am, a "Class 11" radionuclide must also be calculated. This will provide a flux defined in terms of a glass and exchange volume release, e.g., as above, $J_{241\,Am} \approx (J_{11}^{e} + J_{11}^{g}) \times N_{241\,Am}$ where J_{11}^{e} and J_{11}^{g} are the exchange volume and melt glass fluxes per mole of inventory of a "Class 11" radionuclide (Table 3.1) and $N_{241\,Am}$ is the molar inventory of ^{241}Am (e.g., from Table 2.2). Again, because ^{241}Am has a short half life and is involved in an important decay chain, its flux must be corrected for decay, and this will lead to an additional component of ^{237}Np ingrowth of, or more specifically an additional component of ^{237}Np flux ingrowth, which we will denote by J_{Np}^{3}. This may be calculated in terms of $J_{241\,Am}$ using the Bateman Equations (Friedlander et al., 1981):

$$J_{237\,Np}^{3} \approx \left(\frac{\lambda_{241Pu}}{\lambda_{241\,Am} - \lambda_{241Pu}} e^{-\lambda_{241\,Am} t} + \frac{\lambda_{241Pu}}{\lambda_{241Pu} - \lambda_{241\,Am}} \right) \cdot J_{241\,Am}$$

where the decay rates (λ) of both ^{241}Pu and ^{241}Am appear.

Thus, the complete flux of ^{237}Np is given by

$$J_{237\,Np} \approx J_{237\,Np}^{1} + J_{237\,Np}^{2} + J_{237\,Np}^{3}. \tag{4.6}$$

5. Application to Radionuclide Fluxes at CAMBRIC

Consider, now, the release of ^{241}Am and ^{155}Eu from the CAMBRIC test using the simplified model and their comparison with the predictions from the CAMBRIC source term report (Tompson et al., 1999). For reasons explained in Appendix D, only the ^{241}Am flux calculation will be reviewed here. Unless otherwise mentioned, all page and table references pertaining to Tompson et al. (1999) below will be referenced as "TBP."

- **Inventory and Partitioning of ^{241}Am.** For this problem, we can work with the inventories that were used in TBP, as opposed to the average Frenchman Flat values in Table 2.2. As discussed in Table 5 of TBP (p. 23), we have $N = 5.2 \times 10^{-2}$ moles of ^{241}Am. Table 1 of TBP (p. 9) indicates that 95% of this inventory ($N_g = 4.9 \times 10^{-2}$ moles) is sequestered in the melt glass while the remaining 5% ($N_g = 2.6 \times 10^{-3}$ moles) is distributed within the exchange volume. This partitioning is reiterated in Table 9 of TBP (p. 35).
- **Exchange volume.** The exchange volume has a radius of 18 m (p. 25, TBP) and the internal porosity specified within the volume is 0.40 (Table 12, p. 59, TBP). Thus, the bulk volume of the exchange volume is $V_e = 24{,}429$ m^3.
- **Initial concentration in exchange volume.** In the CAMBRIC source term report, ^{241}Am was assumed to be nonsorbing so that it migrates in the absence of retardation effects. Thus, the initial aqueous concentration of ^{241}Am is found by dividing N_e into the available pore volume of V_e, yielding $c_{Am} = 2.66 \times 10^{-7}$ mol/m^3 (Table 12, p. 59, TBP).
- **Groundwater flow through exchange volume and melt glass zone.** The total groundwater flux passing through the melt glass and exchange volume, as derived from the total groundwater flux passing through all 809 modeled streamlines (p. 105, TBP), is

$$Q = \phi \cdot |\mathbf{v}| \cdot A \approx \phi_e \cdot |\mathbf{v}_e| \cdot A_e = 615 \text{ m}^3/\text{y} \ . \tag{5.1}$$

  This value can be used to approximate the flux through the exchange volume since $V_g << V_e$. We can also approximate A_e from the 2/3 power of V_e to get $A_e = 842$ m^2, which, suggests from (5.1) that $|\mathbf{v}_e| \approx 1.82$ m/y.
- **Half lives.** The half-life of ^{241}Am is 433 years (Table 2.2 above).
- **Exchange volume flux component.** Under no-decay conditions, the predicted flux from the exchange volume is a "pulse" of magnitude

$$J_e = Q c_{Am} = 1.64 \times 10^{-4} \text{ mol/y} \tag{5.2a}$$

that will be in effect for a period of

$$\Delta t = \frac{V_e^{1/3}}{|\mathbf{v}_e|} = 15.9 \text{ years} \quad . \tag{5.2b}$$

Note that the product of these two quantities equals the specified exchange volume inventory, N_e.

If the control plane is directly adjacent to the exchange volume (as pictured in Figure 3.2), then the flux pulse begins "at t = 0." If the control plane is located down gradient from the exchange volume, then the flux pulse will have a delayed arrival. In the CAMBRIC simulations, the control plane was located approximately $s_p \approx 180$ m downgradient of the working point of the test. Since the exchange volume mass is distributed within a "cube" of length $V_e^{1/3}$ centered on the working point, the first arrival should occur at

$$t = \frac{s_p - \left(V_e^{1/3}/2 \right)}{|\mathbf{v}_e|} \approx 90 \text{ y} \quad . \tag{5.3}$$

This particular "delayed" flux result—corrected for decay—can be seen as the pulsed release in Figure 5.1 below. The lack of a smeared and dispersed profile, as evident in the Am results of the CAMBRIC simulations (e.g., Figures 51, 52, or 58 on pp. 122, 124, 128, respectively, TBP) is due, in part, to a lack of dispersion in the analytic model and the fact the simulated exchange volume was a sphere and not a cube.

- **Alternative exchange volume flux component.** As an alternative, the classical result in Equation 5.2 above can be evaluated with $N_e = 2.6 \times 10^{-3}$ moles of Am located at the working point, $s_p \approx 180$ m upgradient of the control plane. Some typical results based upon a longitudinal macrodispersivity (α_L) of 17 m (TBP) and the aforementioned velocity magnitude, $|\mathbf{v}_e| \approx 1.82$ m/y, are shown in Figure 5.1 below. This result, of course, will not account for the effects of a spatially distributed initial pulse, nor any "non-classical" dispersion phenomena that may have been produced in the detailed CAMBRIC source term simulations.
- **Melt glass dissolution rate.** As discussed on page 50, TBP, the constant melt glass dissolution rate used in the CAMBRIC source term simulations is[5]

$$k^{\text{mod}} \approx 10^{-13.36} \text{moles-glass/m}^2\text{-s} \tag{5.4}$$

This result is based upon a glass "formula weight" of $f_g = 10{,}000$ g/mole.

[5] This value differs, to some extent, from the more current values proposed in Appendix C, but is used here in support of the overall CAMBRIC comparison effort.

- **Melt glass volume, mass, and surface area.** The mass of melt glass mass used in the CAMBRIC simulations was 905 metric tons, or 9.05×10^8 g of glass (p. 93)[6]. This is equivalent to 9.05×10^4 moles of glass (when f_g = 10,000 g/mole) or 9.05×10^6 moles of glass (when f_g = 100 g/mole)[7].

  The bulk volume of glass (V_g) is approximately 402 m^3, which, based upon the assumed porosity of 0.1 (TBP), yields 362 m^3 of pure glass, or close to 905 metric tons using a glass density of 2.5 g/cm^3.

  The specific surface area per unit mass of the glass (A_s^m) pertaining to Runs 10, 11, or 12 of the CAMBRIC simulations (e.g., Figs. 51, 52, or 58 on pp. 122, 124, 128, respectively, TBP) is 0.52 cm^2/g, or 5.2×10^{-5} m^2/g (p. 42)[8]. The corresponding specific surface area per unit volume of the glass (A_s) is approximately 118 m^2/ m^3 (p. 48, TBP).

- **Predicted melt glass flux.** The melt glass flux predicted using Equation 3.10 is thus

$$J_g \approx f_g \cdot N_g \cdot A_s^m \cdot k^{\text{mod}}$$

$$= (10{,}000 \text{ g/mole})(4.9 \times 10^{-2} \text{ mole})(5.2 \times 10^{-5} \text{ m}^2/\text{g})(10^{-13.36} \text{ mol/m}^2\text{-s})$$

$$= 1.11 \times 10^{-15} \text{ mol/s}$$

$$= 3.51 \times 10^{-8} \text{ mol/y} \qquad (5.5a)$$

  The same result may be obtained with the representation in Equation 3.11 above. Noting that

$$\nu = \frac{4.9 \times 10^{-2} \text{ moles Am}}{9.05 \times 10^4 \text{ moles glass}} = 5.41 \times 10^{-7}$$

  we obtain

$$J_g \approx \nu \cdot V_g \cdot A_s \cdot k^{\text{mod}}$$

---

[6] In TBP, this was computed from a correlation suggesting that approximately 700 to 1,300 metric tons of glass are produced per kiloton of yield (where 1,200 was specifically used). It differs from the recommended 700 tons of glass per kiloton of yield indicated above and in Pawloski (1999) but is used here in support of the overall CAMBRIC comparison effort.

[7] It is somewhat confusing that different values of f_g can be found in the CAMBRIC simulation report (Tompson et al., 1999). Although 10,000 g/mole were used directly in the simulations (e.g., Equation 4), the 100-g/mole figure was used in several supporting calculations (e.g., Table 8).

[8] This value again differs from the suggested surface area range described in Appendix C but is used here in support of the overall CAMBRIC comparison effort.

$$= (5.41 \times 10^{-7})(402\ m^3)(118\ m^2/\ m^3)\ (10^{-13.36}\ mol/m^2\text{-}s)$$
$$= 1.12 \times 10^{-15}\ mol/s$$
$$= 3.54 \times 10^{-8}\ mol/y\ . \qquad (5.5b)$$

5.1 The Combined Picture

The combined exchange volume and melt glass releases predicted from Equations 5.2 and 5.5 above—subsequently corrected for radioactive decay—are shown in Figure 5.1. The analogous ^{241}Am release predicted from the CAMBRIC source term simulations is also shown for comparison. At first glance, three key observations can be made:

- The "pulsed" nature of the exchange volume release is distinct from the dispersed nature of the simulated exchange volume release. This is largely due to the fact that dispersion effects were not included in Equation 5.2 above. This can be addressed, approximately, by using an alternate result such as Equation 3.4 above.
- The arrival time of the (peak) exchange volume release is somewhat later that the corresponding peak arrival in the simulations. This is likely due to the fact that the flux in Equation 5.1 above—used to approximate the mean velocity of the pulse—was affected by slower flows in the melt glass. There may also have been some inconsistencies in reporting the actual control plane location (s_b) past which the simulated flux results were recorded. This will be checked further.
- The magnitude of the **predicted** melt glass release flux is over an order of magnitude lower that the **apparent** melt glass release flux from the simulations, as identified by the tail in the release curve. It is not immediately clear why this is the case. This issue is discussed in the next section.

5.2 Some Realities of the CAMBRIC Simulations that Further Confused Interpretation

As described in Appendix D, there were two errors in the CAMBRIC source term report that made comparison of the simulation results with the simplified source term predictions difficult. To review, let us reconsider the discrepancy between the **predicted** melt glass flux of ^{241}Am (e.g., Equation D.1 in Appendix D below) and the **apparent** melt glass flux in the tail of Figure 5.1, as produced in the simulations. After a bit of research, we now believe there is really no discrepancy between the melt glass flux predicted by the simplified source term model and by the simulations. Consider the following observations:

- Integration of the simulated ^{241}Am flux profile in Figure 5.1 over the 600 years of results produces a total of 2.45×10^{-3} moles of ^{241}Am. This amount is smaller than the exchange volume inventory of 2.6×10^{-3} moles—specified correctly in the simulation—and indicates that not all of the exchange volume inventory has exited the domain after 600 years.

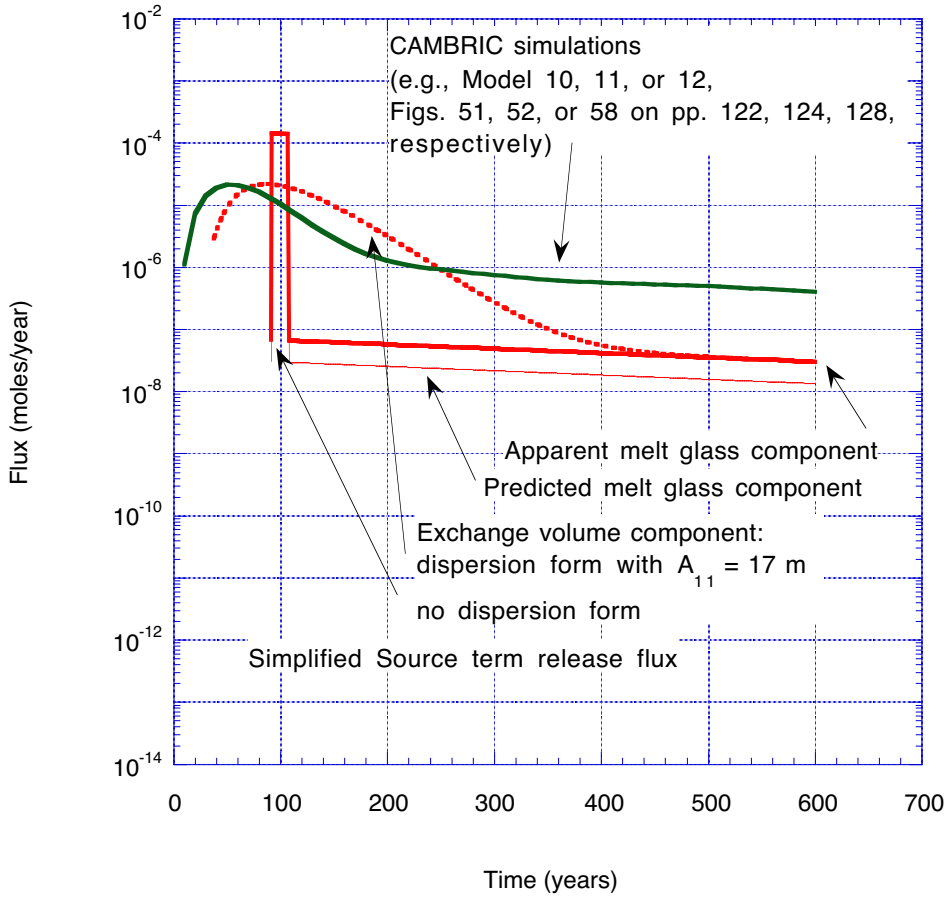

Figure 5.1. Simplified source term release flux for ^{241}Am, as determined for the CAMBRIC test, assuming no retardation. Green curve corresponds to simulated results (Tompson et al., 1999, Figs. 51, 52, or 58). Red curves correspond to simplified analytic results. Exchange volume release components may represent pulsed or dispersed characteristics. Melt glass release components may represent the predicted or apparent (as simulated, yet incorrect) melt glass inventories.

- Analysis of the archived Line 145 data for the Model 12 result of the CAMBRIC simulations indicates that very little (<<1%) of the melt glass along this line has dissolved over the 600 years of the simulation.
- Analysis of archived ^{99}Tc flux results from the classified Frenchman Flat simulations (Pawloski et al., 2000) shows elution behavior that is similar to the Am results of the CAMBRIC simulations in Figure 5.1 above. In the classified simulations, ^{99}Tc is partitioned similarly to ^{241}Am and is unretarded (similar to the way ^{241}Am is treated in the CAMBRIC simulations). But, because the streamline flux results in the classified work were collected and separated into their "glass" and "non-glass" components, we could verify that the long-term tailing behavior evident for ^{241}Am (in Figure 5.1) also exists for the ^{99}Tc results. We also verified that much of this tailing behavior can now

be attributed to long-term elution of the exchange volume portion of the inventory. The melt glass contributions exist, of course, but are about an order of magnitude smaller, similar to what we apparently see in Figure 5.1 above. This suggests that what we call the "apparent" melt glass component of the simulated ^{241}Am flux in Figure 5.1 (from the CAMBRIC results) is largely still an exchange volume component. Thus, it is inappropriate to assert that the so-called "discrepancy" in the simplified melt glass flux prediction is really an error. What we are apparently seeing is a non-classical or non-local dispersion phenomenon related to the way in which radionuclides in the exchange volume were originally distributed into zones of high and low permeability.

5.3 Another Simple Test Problem

To address this last point further, we have created a one-dimensional test problem involving a 50-m-long domain in which the first 10 meters is considered "melt glass" and the remaining 40 meters is considered inert (non sorbing) alluvium. The cross sectional area of this system is 1 m^2. We have assumed that a uniform porosity of 10% exists throughout the domain and that the mean seepage velocity through the system is 1.0 m/y. Although the absolute inventories are different, the initial radionuclide (stoichiometric) composition (e.g., as in Equation 4 of the CAMBRIC report, TBP), melt glass surface area, and constant melt glass dissolution rates are **exactly** as specified in the CAMBRIC simulations. There is no "exchange volume" associated with this problem, so that no ^{241}Am is placed into to any initial aqueous form.

Here, we are concerned with the dissolution of ^{241}Am from the melt glass, its ultimate elution past the 50-m point in the domain, and how a reactive transport simulation of this problem (made with the same code used in the CAMBRIC simulations) compares with the predictions of the simplified source term model. The melt glass flux, calculated with Equation 3.11 above, is[9]

$$J_g \approx \nu \cdot V_g \cdot A_s \cdot k^{\mathrm{mod}}$$

$$= (1.2 \times 10^{-6})(10\ \mathrm{m}^3)(118\ \mathrm{m}^2/\mathrm{m}^3)\ (10^{-13.36}\ \mathrm{mol/m^2\text{-}s})$$

$$= 6.18 \times 10^{-17}\ \mathrm{mol/s}$$

$$= 1.95 \times 10^{-9}\ \mathrm{mol/y}. \qquad (5.6)$$

Initial breakthrough effects notwithstanding, this result compares extremely well with the simulated results for the same problem, as shown in Figure 5.2 below. This suggests that the Simplified Hydrologic Source Term results are adequate for the simplified conditions under which they were derived.

[9] Compare value of ν with that in Equation 5.5b above and see discussion in Appendix D.

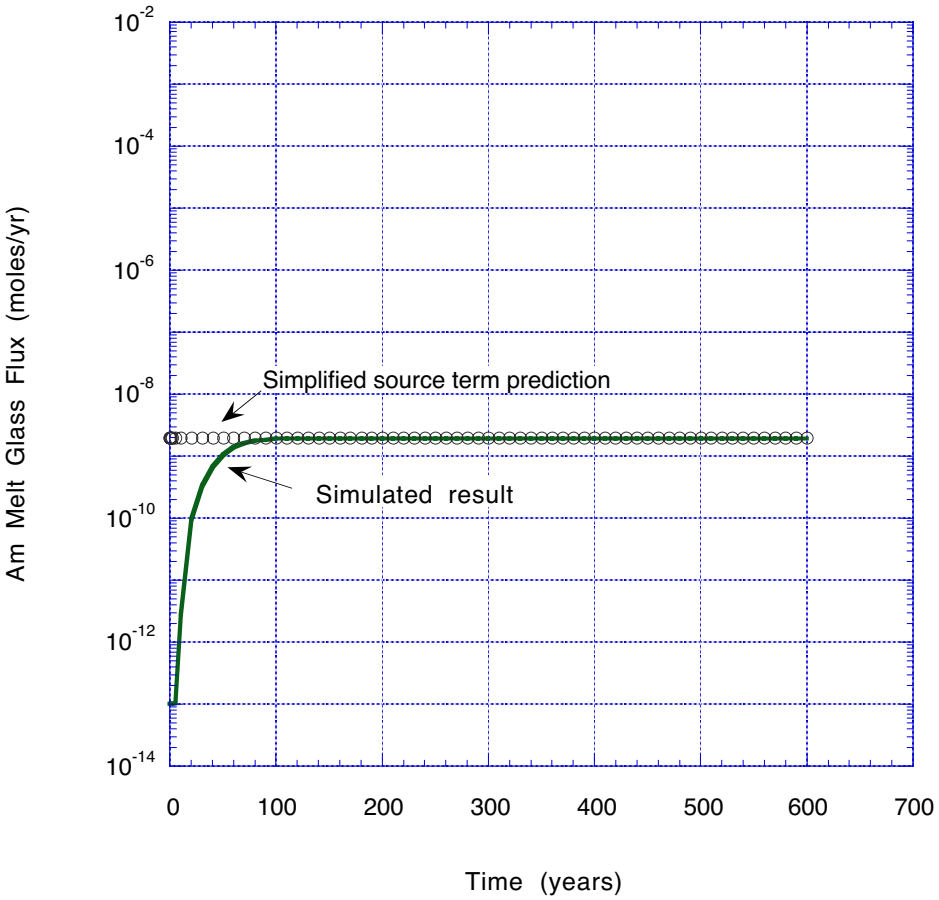

Figure 5.2 Comparison of melt glass release of Am in a simple one-dimensional test problem, with no decay correction. "Simulation" obtained from reactive transport simulation equivalent to what was used in the CAMBRIC report. Simplified source term prediction reproduces this well, initial breakthrough effects notwithstanding.

5.4 Summary

Thus, in summary,

- Comparison of the Simplified Hydrologic Source Term results with the CAMBRIC simulation results was made difficult because of several errors uncovered in the simulations and because the nature of the long-term simulated flux profiles was not wholly understood. Apparently, much of the longer-term elution behavior is still dominated by continued elution of the exchange volume radionuclides—as opposed to melt glass dissolution only. This is non-classical dispersion behavior that could not captured by the classical model in Equation 3.1 above.
- After a thorough evaluation, it appears that the Simplified Hydrologic Source Term does provide reasonable results that are valid for the conditions under which it was derived.

- It would also appear that incorporation of diffusion or macrodispersion effects in the exchange volume component of the Simplified Hydrologic Source Term may be warranted; one approach was suggested here, and there may be others.

6. Further Sensitivity Studies

Although we used unclassified data to approximate all test-related parameters, we realize that the current results do not systematically cover the full range of variability that may be used in a proper sensitivity analysis. Below, we summarize some of the more important variations that we suggest be considered in such an analysis.

6.1 Test volumes

We grouped the tests and their parametric and volumetric information (Table 2.1) into three important **groups.** The size of the exchange volume is estimated in terms of the cavity radius, R_c, which is, itself, approximated from a calculation based on test yield, overburden bulk density, and depth of burial. If V_e were modified because of uncertainty in the yield or other parametric measurements used to calculate R_c (over specified ranges), then

- Different groupings of test may be established;
- Initial aqueous molar concentrations listed in Table 3.2 would differ, and, as a result,
- Radionuclide fluxes out of the exchange volume would change.

In addition, the exit area A_e on the breakthrough plane, across which the fluxes are determined, will also be affected by the size of the exchange volume.

6.2 Radionuclide Inventory

The list of radionuclides (Table 2.2) and their initial inventories (Tables 2.2 and 3.1) are approximate and their variation or modification as a result of new information will clearly affect the flux results. Variations in the radionuclide list, the radionuclide **class** assignments (Table 3.2), or the initial molar inventories could be examined in a sensitivity analysis. In addition, the impacts and importance of decay and ingrowth (Section 2.3) will be highly dependent on the relative abundance of the various radionuclides in the important decay chains.

6.3 Retardation Effects

The chemical retardation data are uncertain and ranges in K_d^i (and, therefore, R_i) values have been provided in Tables 3.1, D–3, and D-4. These parameters directly affect the initial aqueous concentrations listed in Table 3.2, the magnitude of the exchange volume fluxes (Eq. 3.2), as well as the relative time (t_{max}) over which exchange volume releases may be observed (Section 3.3). The lack of retardation data for select radionuclides (treated otherwise as tracers in Table 3.1) should not be forgotten. Clearly, alternative versions of Table 3.2 could be constructed for Frenchman Flat alluvium based upon a goethite form of iron oxide, or to reflect the effects of higher or lower values of the K_d^i (or, R_i) parameter ranges.

6.4 Melt Glass Release

The melt glass release (Eq. 3.9) will be heavily controlled by the specific surface area A_S^m and modified glass dissolution constant k^{mod} parameters employed in the calculation, and the fact that they are assumed to be constant. Appendix C summarizes several important caveats associated with this assumption and suggests several viable ranges for the parameters that are used in the Simplified Source Term Model.

7. Summary

The purpose of this report was to provide an unclassified simplification of the hydrologic source term (HST) for the ten underground nuclear tests conducted in the Frenchman Flat Corrective Action Unit (CAU) at the Nevada Test Site (NTS). It was developed from the results of more complex source term modeling studies at Frenchman Flat and Pahute Mesa at NTS. The HST of a specific underground test represents the time-release or flux of test related radionuclides into groundwater, away from the underground testing point. It is a function of

- The radionuclide inventory.
- The spatial distribution of this inventory about the working point of the test.
- The fractionation of this inventory between melt glass and non-melt glass zones about the working point of the test.
- The rate of groundwater flow through the initially contaminated zones surrounding the test.
- The chemical mobility of the radionuclides in groundwater.
- The radionuclide decay characteristics of the radionuclides.

Many of these characteristics can be estimated from the yield and depth of burial of each test and knowledge of the relevant radionuclide inventories, which, for the purposes of this report, can only be estimated using unclassified information. Unclassified information on test yields and the entire Frenchman Flat radionuclide inventory were applied in this report for these purposes.

Many features of the release functions used in this report are admittedly approximate and have been simplified for easy use. Principal assumptions include:

- The temperature is assumed fixed so that the impacts of residual test-related heat are not considered.
- Groundwater flow is considered steady and the groundwater pH is assumed constant.
- Radionuclide release from the melt glass is assumed to occur at a fixed rate.
- Chemical sorption (via ion exchange and surface complexation) is assumed to be described by simple retardation coefficients that are functions of the geologic medium and ambient groundwater chemistry.
- Radionuclide mineral precipitation/dissolution and formation of radionuclide-sorbing minerals in the melt glass or elsewhere is ignored.

Numerous examples of the simplified source term were presented. In particular, the predicted release of ^{241}Am from the CAMBRIC test using the results of this report compare well with the previous results of Tompson et al. (1999). Two important errors in the report of Tompson et al. (1999) are also clarified and discussed.

Acknowledgements

This work was performed under the auspices of the U. S. Department of Energy by the University of California, Lawrence Livermore National Laboratory (LLNL) under contract W-7405-Eng-48. This work was supported by the Underground Test Area Project, U. S. Department of Energy, National Nuclear Security Administration, Nevada Site Office. We are grateful for the reviews and comments of Jeffrey Daniels and David Smith.

8. References

Aagaard, P., and H. C. Helgeson (1982), Thermodynamic and kinetic constraints on reaction rates among minerals and aqueous solutions, I. Theoretical considerations. American Journal of Science 282, 237–285.

Baxter, R. G. (1983), Description of Defense Waste Processing Facility Reference Form and Canister: Savannah River Plant, Savannah River, Georgia. Report No. DP-1606, rev. 1.

Borg, I., R. Stone, H. B. Levy, and L. D. Ramspott (1976), Information pertinent to the migration of radionuclides in ground water at the Nevada Test Site. Part 1: Review and analysis of existing information, Lawrence Livermore National Laboratory, Livermore, CA (UCRL-52078).

Bourcier, W. L., S. Roberts, D. K. Smith, S. Hulsey, L. Newton, A. Sawvel, C. Bruton, C. Papelis, W. Um, C. Russell, and J. Chapman, (2001), Determination of reactive surface area of melt glass,, Lawrence Livermore National Laboratory, Livermore, CA (UCRL-ID-145181).

Bourcier, W. L. (1994), Critical review of glass performance modeling, Argonne National Laboratory, Argonne IL (ANL-94/17).

Bowen, S. M., D. L. Finnegan, J. L. Thompson, C. M. Miller, P. L. Baca, L. F. Olivas, C. G. Geoffrion, D. K. Smith, W. Goishi, B. K. Esser, J. W. Meadows, N. Namboodiri, and J. F. Wild (2001), Nevada Test Site Radionuclide Inventory, 1951–1992, Los Alamos National Laboratory, Loa Alamos, NM (LA-13859-MS)

Bradbury, M. H. and B. Baeyens (1997), A mechanistic description of Ni and Zn sorption on Na-montmorillonite .2. Modeling. Journal of Contaminant Hydrology, 27(3-4): 223-248.

Carslaw, H. S., and J. C. Jaeger. (1986), Conduction of heat in solids, 2nd ed., Oxford University Press, New York, 510 p.

Chipera, S. J. and D. L. Bish (1989), Quantitative x-ray diffraction analyses of samples used for sorption studies by the Isotope and Nuclear Chemistry Division, Los Alamos National Laboratory. Los Alamos National Laboratory, Los Alamos, NM (LA-11669-MS).

Daniels, W. R., J. L. Thompson (1984), Laboratory and Field Studies Related to the Radionuclide Migration Project, October 1, 1982 to September 30, 1983. Los Alamos National Laboratory, Los Alamos, NM (LA-10121-PR).

Daniels, J. I., A. F. B. Tompson, D. K. Smith, and M. Zavarin (2001), Development of a comprehensive radiologic source term (RST) – Application to the CHESHIRE Site, Lawrence Livermore National Laboratory, Livermore, CA (UCRL-MI-143412), Official Use Only.

Davis, J. A., J. A. Coston, D. B. Kent and C. C. Fuller (1998), Application of the surface complexation concept to complex mineral assemblages. Environmental Science & Technology, 32(19): 2820-2828.

Duff, M. C. and C. Amrhein (1996), Uranium(VI) adsorption on goethite and soil in carbonate solutions. Soil Science Society of America Journal, 60(5): 1393-1400.

Duff, M. C. et al., (1999), Mineral associations and average oxidation states of sorbed Pu on tuff. Environmental Science & Technology, 33(13): 2163-2169.

Dzombak, D. A. and F. M. M. Morel (1990), Surface complexation modeling : hydrous ferric oxide. Wiley, New York, xvii, 393 pp.

FFACO (1996), Federal Facilities Agreement and Consent Order. Agreed to by the U. S. Department of Energy, the U.S. Department of Defense, and the State of Nevada, Las Vegas, NV

FFACO (2000), Federal Facilities Agreement and Consent Order, Appendix VI, December 7, 2000; Revision 1; Agreed to by the U. S. Department of Energy, the U.S. Department of Defense, and the State of Nevada, Las Vegas, NV.

Friedlander, G., J. Kennedy, E. Macias, and J. Miller (1981), Nuclear and Radiochemistry, 3rd ed., John Wiley and Sons, New York, NY.

Gelhar, L. W., and M. A. Collins (1971), General analysis of longitudinal dispersion in nonuniform flow, Water Resources Research 7(6), 1511-1521.

Golder Associates (2000), User's Guide, GoldSim, Graphical Simulation Environment. Version 6.02. Manual Draft #4 (March 17, 2000). Redmond, Washington: Systems Simulation Group, Golder Associates. TIC: 247347.

Hoffman, D. C., R. Stone, and W. W. Dudley, Jr. (1977), Radioactivity in the underground environment of the CAMBRIC nuclear explosion at the Nevada Test Site, Los Alamos National Laboratory, Los Alamos, NM (LA-6877-MS).

Hsi, C. D. and D. Langmuir (1985), Adsorption of uranyl onto ferric oxyhydroxides; application of the surface complexation site-binding model. Geochimica et Cosmochimica Acta, 49(9): 1931-1941.

IAEA (1998a), The radiological situation at the atolls of Mururoa and Fangataufa. Technical report, Volume 3. Inventory of radionuclides underground at the atolls. International Atomic Energy Agency, Vienna, Austria (IAEA-MFTR-3).

IAEA (1998b), The radiological situation at the atolls of Mururoa and Fangataufa. Technical report, Volume 4. Releases to the biosphere of radionuclides from underground nuclear weapons tests at the atolls. International Atomic Energy Agency, Vienna, Austria (IAEA-MFTR-4).

Jones, B. F. (1982), Mineralogy of Fine Grained Alluvium from Borehole U11g, Expl. 1, Northern Frenchman Flat Area, Nevada Test Site. U.S. Geological Survey, Open-File Report 82-765.

Keeney-Kennicutt, W. L. and J. W. Morse (1984), The interaction of Np(V)O2+ with common mineral surfaces in dilute aqueous solutions and seawater. Marine Chemistry, 15: 133-150.

Keeney-Kennicutt, W. L. and J. W. Morse (1985), The redox chemistry of Pu(V)O2+ interaction with common mineral surfaces in dilute solutions and seawater. Geochimica et Cosmochimica Acta, 49(12): 2577-2588.

Kinzelbach, W. (1988), The random walk method in pollutant transport simulation, in Groundwater Flow and Quality Modeling, E. Custodio et al., Eds., Kluwer Academic Publishers, Dordrecht, 227–245.

Koeppenkastrop, D. and E. H. Decarlo (1992), Sorption of Rare-Earth Elements From Seawater Onto Synthetic Mineral Particles - an Experimental Approach. Chemical Geology, 95(3-4): 251-263.

Krishnaswami, S., W. C. Graustein, K. K. Turekian, and J. F. Dowd (1982), Radium, thorium, and radioactive lead isotopes in groundwaters: Application to the in situ determination of adsorption-desorption rate constants and retardation factors. Water Resources Research, 18(6): 1663-1675.

Kurbatov, M. H., Wood, G.B. and J. D. Kurbatov (1951), Isothermal adsorption of cobalt from dilute solutions. Journal of Physical Chemistry, 55: 1170-1182.

Maxwell, R. M., A. F. B. Tompson, J. T. Rambo, S. F. Carle, and G. A. Pawloski (2000), Thermally induced groundwater flow resulting from an underground nuclear test, in Computational Methods in Water Resources XIII, Volume 1. L. Bentley, J. Sykes, C. Brebbia, W. Gray, and G. Pinder (eds.), A. A. Balkema Publishers, Rotterdam, 45–50.

McKinley, J. P., J. M. Zachara, S. C. Smith, and G. D. Turner (1995), The influence of uranyl-hydrolysis and multiple site-binding reaction on adsorption of U(VI) to montmorillonite. Clays and Clay Minerals, 45(5): 586-598.

Moore, R. M. and Hunter, K. A. (1985), Thorium adsorption in the ocean: Reversibility and distribution amongst particle sizes. Geochimica et Cosmochimica Acta, 49: 2253-2257.

Nitsche, H. et al., (1993), Measured solubilities and speciations of neptunium, plutonium, and americium in a typical groundwater (J-13) from Yucca Mountain region. Los Alamos National Laboratory, Los Alamos, NM (LA-12562-MS).

Pawloski, G. A. (1999), Phenomenological models of underground nuclear tests–BENHAM and TYBO), Lawrence Livermore National Laboratory, Livermore, CA (UCRL-ID-136003).

Pawloski, G. A., A. F. B. Tompson, C. J. Bruton, and M. Zavarin, eds. (2000), Evaluation of the hydrologic source term from underground nuclear tests in Frenchman Flat at the Nevada Test Site (U), Lawrence Livermore National Laboratory, Livermore, CA (UCRL-ID-138007-DR).

Pawloski, G. A., A. F. B. Tompson, and S. F. Carle, eds. (2001), Evaluation of the hydrologic source term from underground nuclear tests on Pahute Mesa at the Nevada Test Site; The CHESHIRE test, Lawrence Livermore National Laboratory, Livermore, CA (UCRL-ID-147023).

Ramspott, L.D., McArthur, R.D. (1977), Results of the Exploratory Drill Hole Ue5n, Frenchman Flat, Nevada Test Site. Lawrence Livermore National Laboratory. Livermore, CA (UCID-17392).

Sawyer, D. A., J. L. Thompson, and D. K. Smith (1999), The CHESHIRE migration experiment: A summary report, Los Alamos National Laboratory, Los Alamos, NM (LA-13555-MS).

Schwartz, L., A. Piwinski, F. Ryerson, H. Tewes, and W. Beiringer (1984), Glass produced by underground nuclear explosions. In P. L. D., J. A. O'Keefe, and V. D. Frechette (eds.), Natural Glasses, p. 559-598. North Holland, Amsterdam.

Smith, D. K. (1995), Characterization of nuclear explosive melt debris, Radiochimica Acta 69, 157–167.

Smith, D. K. (2001), Unclassified Radiologic Source Term for Nevada Test Site Areas 19 and 20, Lawrence Livermore National Laboratory, Livermore, CA (UCRL-ID-141706).

Thomas, K. W. (1987), Summary of sorption measurements performed with Yucca Mountain, Nevada Tuff Samples and water from well J-13. Los Alamos National Laboratory, Los Alamos, NM (LA-10960-MS).

Tompson, A. F. B., C. J. Bruton, and G. A. Pawloski, eds. (1999), Evaluation of the hydrologic source term from underground nuclear tests in Frenchman Flat at the Nevada Test Site: The CAMBRIC test, Lawrence Livermore National Laboratory, Livermore, CA (UCRL-ID-132300).

Tompson, A. F. B., C. J. Bruton, G. A. Pawloski, D. K. Smith, W. L. Bourcier, D. E. Shumaker, A. B. Kersting, S. F. Carle, and R. M. Maxwell (2002), On the Evaluation of Groundwater Contamination from Underground Nuclear Tests, Environmental Geology, 42, 235-247.

Turner, G. D., Zachara, J.M., McKinley, J.P. and Smith, S.C., (1996), Surface charge properties and UO22+ adsorption of a subsurface smectite. Geochimica et Cosmochimica Acta, 60(18): 3399-3414.

USDOE (1999), Corrective Action Investigation Plan for Corrective Action Unit 98: Frenchman Flat, Nevada Test Site, Nevada, U.S. Department of Energy, Nevada Operations Office, Las Vegas, NV (DOE/NV--478-REV 1).

USDOE (2000), United States Nuclear Tests: July 1945 through September 1992, U.S. Department of Energy, Nevada Operations Office, Las Vegas, NV (DOE/NV--209; Rev 15).

Vaniman, D., Furlano, A., Chipera, S., Thompson, J. and Triay, I. (1995), Microautoradiography in studies of Pu(V) sorption by trace and fracture minerals in tuff. In: W.M. Murphy and D.A. Knecht (Editors), Scientific Basis for Nuclear Waste Management XIX. Material Research Society, Pittsburgh, pp. 639-646.

Viani, B. E. and Bruton, C. J. (1992), Modeling fluid-rock interaction at Yucca Mountain, Nevada: A progress report. Lawrence Livermore National Laboratory, Livermore, CA (UCRL-ID-109921).

Viani, B. E. and Bruton, C. J., (1996), Assessing the role of cation exchange in controlling groundwater chemistry during fluid mixing in fractured granite at Aspo, Sweden., Lawrence Livermore National Laboratory, Livermore, CA (UCRL-JC-121527).

Wadman, R. E. and W. D. Richards (1961), Postshot geologic studies of excavations below RAINIER ground zero, Lawrence Livermore National Laboratory, Livermore, CA (UCRL-6586).

Walker, F. W., J. R. Parrington, and F. Feiner (1989), Nuclides and Isotopes, Fourteenth Edition—Chart of the Nuclides, GE Nuclear Energy, General Electric Company, Nuclear Energy Operations, San Jose, CA.

Warren, R. G., D. A. Sawyer, F. M. Byers, Jr., and G. L. Cole (2000), A petrographic/geochemical database and stratigraphic framework for the southwestern Nevada volcanic field, in preparation, future revision to Los Alamos National Laboratory , Loa Alamos, NM (LA-UR-00-3791).

Wild, J. F., W. Goishi, J. W. Meadows, M. N. Namboodiri, and D. K. Smith (1998), The LLNL Nevada Test Site Underground Radionuclide Source-Term Inventory, in Atmospheric Nuclear Tests—Environmental and Human Consequences, C. S. Shapiro, Ed. (Springer-Verlag, Berlin, Germany), NATO ASI Series, Partnership Sub-Series, 2. Environment–Volume 35, 69–77.

Wolfsberg, K. (1978), Sorption-Desorption Studies of Nevada Test Site Alluvium and Leaching Studies of Nuclear Test Debris. Los Alamos National Laboratory, LA-7216-MS

Zachara, J. M., Cowan, C. E. and Resch, C.T., (1993), Metal cation/anion adsorption on calcite carbonate. In: H.E. Allen, E.M. Perdue and D.S. Brown (Editors), Metals in groundwater. Lewis Publishers, Boca Raton, pp. 37-71.

Zachara, J. M., Resch, C. T. and Smith, S.C., (1994), Influence of humic substances on Co2+ sorption by a subsurface mineral separate and its mineralogic components. Geochimica et Cosmochimica Acta, 58(2): 553-566

Zavarin, M. and Bruton, C. J., (2000a), A Non-Electrostatic Surface Complexation Approach to Modeling Radionuclide Migration at the Nevada Test Site: Aluminosilicates. Lawrence Livermore National Laboratory, Livermore (UCRL-ID-141840 DR).

Zavarin, M. and Bruton, C. J. (2000b), A Non-Electrostatic Surface Complexation Approach to Modeling Radionuclide Migration at the Nevada Test Site: Iron Oxides and Calcite. Lawrence Livermore National Laboratory, Livermore(UCRL-ID-141841 DR).

Zhong, S. J. and Mucci, A. (1995), Partitioning of rare earth elements (REEs) between calcite and seawater solutions at 25-degrees-C and 1 atm, and high dissolved REE concentrations. Geochimica et Cosmochimica Acta, 59(3): 443-453.

Appendix A: Thirteen Pertinent Decay Chains Associated with the RST

Excluding ^{40}K, Table 2.2 represents a list of 44 primary RST radionuclides deemed relevant for the source term calculation. A total of 21 of these decay directly into stable daughter products and have no parent RST radionuclides. These will not be discussed any further here. An additional four members of the RST decay into short-lived radioactive daughter products, which, in turn, decay into stable granddaughters. These are tabulated below in Section A.1. Finally, the remaining 18 primary RST radionuclides are members of nine additional decay chains. One new daughter product (^{152}Gd) has been identified that may be considered a derivative member of the RST. These will be discussed below in Section A.2 in terms of the relevant decay and ingrowth chains that need to be addressed over a 1,000-year simulation period.

A.1 ^{90}Sr, ^{126}Sn, ^{137}Cs, and ^{232}U Chains

The following four chains are characterized by a parent radionuclide in the RST decaying into a stable, end-member daughter via one or more short-lived intermediary radionuclides, indicated here (and later) in parentheses. Short-lived radionuclides will not be considered further in this report.

$$^{90}\mathrm{Sr} \xrightarrow{29.1\,y/\beta} \left(^{90}\mathrm{Y} \xrightarrow{64\,h/\beta} \right) ^{90}\mathrm{Zr}\ \text{(stable)} \tag{A.1}$$

$$^{126}\mathrm{Sn} \xrightarrow{\sim 10^{5}\,y/\beta} \left(^{126}\mathrm{Sb} \xrightarrow{12.5\,d/\beta} \right) ^{126}\mathrm{Te}\ \text{(stable)} \tag{A.2}$$

$$^{137}\mathrm{Cs} \xrightarrow{30\,y/\beta} \left(^{137\mathrm{m}}\mathrm{Ba} \xrightarrow{2.5\,m/IT} \right) ^{137}\mathrm{Ba}\ \text{(stable)} \tag{A.3}$$

$$^{232}\mathrm{U} \xrightarrow{70\,y/\alpha} \left(^{228}\mathrm{Th} \xrightarrow{1.9\,y/\alpha} 7\ \text{short - lived intermediaries} \longrightarrow \right) ^{208}\mathrm{Pb}\ \text{(stable)} \tag{A.4}$$

In the case of the ^{232}U chain, we assume that ^{228}Th is "short lived."

A.2 Nine Additional Coupled Chains Involving RST Radionuclides

^{93}Zr chain. Both ^{93}Zr and ^{93m}Nb are primary members of the RST. Because of the long half–life of ^{93}Zr the ingrowth of ^{93m}Nb from this reaction over 1,000 years should not be significant, so both can be treated independently in decay and transport calculations.

$$^{93}\mathrm{Zr} \xrightarrow{\sim 10^{6}\ y/\beta} {}^{93m}\mathrm{Nb} \xrightarrow{16.1\ y/IT} {}^{93}\mathrm{Nb\ (stable)} \tag{A.5}$$

^{150}Gd chain. Because ^{150}Gd has such a long half life, it can be considered effectively stable over a 1,000-year analysis:

$$^{150}\mathrm{Gd} \xrightarrow{\sim 10^{6}\ y/\alpha} \cdots \tag{A.6}$$

Subsequent daughter products in this chain are ^{146}Sm (~10^{8} y/α) and ^{142}Nd (stable).

^{152}Eu chain. ^{152}Eu decays in a 72% branch to ^{152}Sm (stable) and in a 28% branch to ^{152}Gd, a derivative radioactive element that was not included in the primary RST list of Bowen et al. (2001). Because ^{152}Gd has such a long half-life, however, it can be considered effectively stable. Ingrowth of ^{152}Gd from ^{152}Eu will be important:

$$^{152}\mathrm{Eu} \xrightarrow{(28\%\ \text{branch})\ 13.5\ y/\beta} {}^{152}\mathrm{Gd} \xrightarrow{\sim 10^{14}\ y/\alpha} \cdots \tag{A.7}$$

Subsequent daughter products produced beyond ^{152}Gd are ^{148}Sm (~10^{16} y/α), ^{144}Nd (~10^{15} y/α), and ^{140}Ce (stable).

^{241}Pu chain. Four of the first five members of this decay chain are included as primary members of the RST. The coupled decay and ingrowth between ^{241}Pu, ^{241}Am, and ^{237}Np must be treated explicitly in a transport model because of their relatively short half-lives. However, since the half–lives of ^{237}Np and ^{233}U are so long, the ingrowth of ^{233}U and subsequent daughters can be effectively excluded in our 1,000-year decay and transport calculations.

$$^{241}\mathrm{Pu} \xrightarrow{14.4\ y/\beta} {}^{241}\mathrm{Am} \xrightarrow{433\ y/\alpha} {}^{237}\mathrm{Np} \xrightarrow{\sim 10^{6}\ y/\alpha} \left({}^{233}\mathrm{Pa} \xrightarrow{\sim 27\ d/\beta} {}^{233}\mathrm{U} \xrightarrow{\sim 10^{5}\ y/\alpha} \cdots \right) \tag{A.8}$$

Notable (but not all) daughter products produced beyond ^{233}U include ^{229}Th (~7,300 y/α) and ^{225}Ra (~15d/β).

^{242}Pu chain. Three members in this chain are primary members of the RST. Because ^{238}U and ^{234}U have relatively long half–lives, ingrowth of ^{234}U and its further decay into additional daughters can be effectively excluded in our 1,000-year decay and transport calculations.

$$^{242}\mathrm{Pu} \xrightarrow{\sim 10^{5}\, y/\alpha} {}^{238}\mathrm{U} \xrightarrow{\sim 10^{9}\, y/\alpha} \left({}^{234}\mathrm{Th} \xrightarrow{\sim 24 d/\beta} {}^{234}\mathrm{Pa} \xrightarrow{\sim 6 h/\beta} \right) {}^{234}\mathrm{U} \xrightarrow{\sim 10^{5}\, y/\alpha} \cdots \quad \text{(A.9)}$$

Notable (but not all) daughter products produced beyond ^{234}U include ^{230}Th (~10^5 y/α), ^{226}Ra (~1600y/α), and ^{222}Rn (4d/α).

^{238}Pu chain. Both ^{238}Pu and ^{234}U are primary members of the RST. ^{238}Pu decays with a relatively short half–life into ^{234}U, whose decay into further daughter products can be effectively ignored in the model because of its long half–life.

$$^{238}\mathrm{Pu} \xrightarrow{87.7\, y/\alpha} {}^{234}\mathrm{U} \xrightarrow{\sim 10^{5}\, y/\alpha} \cdots \quad \text{(A.10)}$$

As above, notable (but not all) daughter products produced beyond ^{234}U include ^{230}Th (~10^5 y/α), ^{226}Ra (~1600y/α), and ^{222}Rn (4d/α).

^{243}Am chain. Three members shown in this chain are primary members of the RST. Because ^{239}Pu and ^{235}U have relatively long half–lives, ingrowth of ^{235}U and its further decay into additional daughters can be safely ignored in our 1,000-year decay and transport calculations.

$$^{243}\mathrm{Am} \xrightarrow{7370\, y/\alpha} \left({}^{239}\mathrm{Np} \xrightarrow{\sim 2 d/\alpha} \right) {}^{239}\mathrm{Pu} \xrightarrow{\sim 10^{4}\, y/\alpha} {}^{235}\mathrm{U} \xrightarrow{\sim 10^{9}\, y/\alpha} \cdots \quad \text{(A.11)}$$

Notable (but not all) daughter products produced beyond ^{235}U include ^{231}Th (~1d/β), ^{231}Pa (~10^4 y/α), ^{227}Ac (22y/β), ^{227}Th (19d/α), ^{223}Ra (11d/α), and ^{219}Rn (4s/α).

^{244}Cm chain. Each member shown in this chain is a primary member of the RST. Although the ingrowth of ^{240}Pu from ^{244}Cm must be accounted for, the half-lives of ^{240}Pu and ^{236}U suggest the ingrowth of ^{236}U, ^{232}Th, and subsequent daughters will not be significant over the 1,000–year time of the model.

$$^{244}\mathrm{Cm} \xrightarrow{18.1\, y/\alpha} {}^{240}\mathrm{Pu} \xrightarrow{6560\, y/\alpha} {}^{236}\mathrm{U} \xrightarrow{\sim 10^{7}\, y/\alpha} {}^{232}\mathrm{Th} \xrightarrow{\sim 10^{10}\, y/\alpha} \cdots \quad \text{(A.12)}$$

Notable (but not all) daughter products produced beyond ^{232}Th include ^{228}Ra (6y/β), ^{228}Ac (6h/β), ^{228}Th (2y/α), ^{224}Ra (4d/α), and ^{220}Rn (1m/α).

Appendix B: Application of Near-Field Surface Complexation and Ion Exchange Models to Linear Retardation Transport Models

Minerals that can exhibit a surface charge (e.g. iron oxides, calcite, aluminosilicates etc.) can significantly reduce the mobility of some radionuclides in groundwater as a result of surface complexation and ion exchange (sorption) reactions. Characterization of these reactions can lead to the development of a mechanistic understanding of how sorption and retardation phenomena are affected or otherwise controlled by changing environmental conditions. In general, the mathematical representation of these reactions may involve a number of complex, nonlinear equilibrium or kinetic constraints that must be satisfied by the concentrations of all chemical species present. Under certain conditions, however, this complex model may be simplified in such a way that linear and independent partitioning (or "K_d") models may be applied for each sorbing species. The conditions required for these simplifications are:

- Invariant solution conditions;
- Radionuclide concentrations well below the point at which reactive surface sites may become saturated;
- Radionuclide concentrations well below the respective mineral precipitate saturations.

The linear retardation coefficients presented below were derived from our non-electrostatic surface complexation and ion exchange database. This database was developed to model the interaction of radionuclides with the surfaces of iron oxides, carbonates, and aluminosilicates (Zavarin and Bruton, 2000a; Zavarin and Bruton, 2000b).

B.1 Implementation of Linear Surface Complexation and Ion Exchange Models

Radionuclide K_d s were determined using the mineralogic conditions and water chemistry defined in the unclassified Cambric report (Tompson et al., 1999). The surface complexation and ion exchange reactions used to define the K_d s are supplemented by more recent analyses of various published and experimental data. A summary of these data can be found in Zavarin and Bruton (2000a; 2000b). The mineralogy of the Frenchman Flat alluvium and the water chemistry are presented in Tables B.1 and B.2 (derived from Tompson et al., 1999). While our simplified K_d approach is expected to accurately forecast radionuclide retardation under these particular conditions, changes in water chemistry due to glass dissolution or other factors, high temperatures near the glass zone at short times, competition for sorption sites, and the heterogeneous distribution of sorbing minerals will all affect radionuclide retardation. Water chemistry changes due to glass dissolution could, for example, increase or decrease $Na^+/K^+/Ca^{2+}/Mg^{2+}$ concentrations, which would affect radionuclide sorption to ion exchange sites. Glass dissolution could also affect the pH, which would affect both the solution chemistry and the protonation on surface complexation sites. Changes in the redox state of near-field groundwater as a result of glass dissolution could severely alter the transport behavior of redox-sensitive elements such as Pu and U. The heterogeneous distribution of sorbing minerals in

Frenchman Flat alluvium will likely create spatially variable radionuclide retardation, which will significantly affect the overall transport of radionuclides. Thus, some care should be taken in applying our K_d values to Frenchman Flat alluvium.

Tables B.3 and B.4 (also plotted in Figures B.1 and B.2) list the K_d s for each sorptive mineral and each radionuclide determined using the water chemistry defined in Table B.2 and mineral surface areas and CECs defined in Table B.1. Included in Tables B.3 and B.4 are K_d s for each radionuclide–mineral pair calculated at ±2 standard deviations of the surface complexation[10]. The uncertainty in the ion exchange reaction constants could not be readily estimated because these data were taken directly from published data (that did not include standard deviations). Thus, in most cases, a standard deviation of 0.5 was assumed. However, for Cs, lower limit ion exchange constants were estimated to equivalence with K for zeolite, smectite, and basal plane illite. Lower limit ion exchange constants were reduced by $\log_{10}$ K of 1.0 for the two illite edge sites. The lower limit ion exchange constant for Sr on zeolite (clinoptilolite) was estimated to equivalence with Ca. Uncertainties in other Sr ion exchange constants and all Ca ion exchange constants were not estimated. The uncertainties in ion exchange constants (Table B.3) are not based on measured uncertainties and are, thus, only useful to demonstrate the potential effects of variable ion exchange affinities on radionuclide transport. The difference between the goethite and hematite K_d s results only from the difference in surface area used to model sorption to these minerals (see Zavarin and Bruton, 2000a; 2000b). Typically, hematite will have a significantly lower surface area than goethite. The use of hematite K_d versus goethite K_d can be used to assess the effect of iron oxide reactive surface area on radionuclide transport. Table B.4 and Figure B.2 present K_d s for Pu at two oxygen fugacities: 10^{-10} and 0.2 bars (saturation with the atmosphere). At the fugacity of 10^{-10}, the dominant Pu redox is in the +5 state while at 0.2, it is in the +6 state. Evidence from Yucca Mountain water experiments (Nitsche et al., 1993, 1994) suggest that Pu(V) should be the dominant Pu redox state in these waters. Thus, we believe that the K_d at $f(O_2) = 10^{-10}$ bars is more realistic. However, the results we show here clearly indicate that Pu in a more oxidized state is likely to be much less retarded (~1 order of magnitude decrease in K_d). Conversely, if the groundwater were to become more reducing, it is likely that Pu migration would decrease significantly because Pu(IV) sorbs more strongly than Pu(V).

[10] For those surface complexation reactions that did not have standard deviations listed, a log K standard deviation of 0.5 was used. Note that log K is not equivalent to $\log_{10} K_d$.

Table B.1. Porous media volume fractions defined for the Frenchman Flat alluvium, based on Tompson et al. (1999).

Solid mineral or pore volume	Density (g/cm^3)	Volume fraction (%)	Surface area (m^2/g)	CEC (meq/g)
Inert Matrix	2.5	47	0	0
Clinoptilolite-Ca	2.13	5	0	2.12
Beidellite-Ca	2.83	5	30	0.85
Calcite	2.71	1	2.2	0
Muscovite	2.83	1	0	0.2[a]
Goethite[b]	4.27	1	50	0
Hematite[b]	5.27	1	2	0
Porosity	–	40	–	–

[a] 3 site types: site I = 0.005, site II = 0.03, site III = 0.965.

[b] The alluvium can be assumed to be dominate by either hematite or goethite but not both. See below for comparisons of hematite-dominated and goethite-dominated alluvium K_ds.

Table B.2. Ambient Frenchman Flat water chemistry used to define K_d s, based on Tompson et al. (1999).

Constituent	Value
pH	8.0
Constituent	**Concentration (mg/L)**
Na	63
K	8
Ca	16
Mg	4
HCO_3	177
Cl	16
SO_4	32
SiO_2	65
$O_2(g)$	8.1, $4.0*10^{-9}$ [a]

[a] Equivalent to $f(O_2) = 0.2$ and 10^{-10}, respectively.

Table B.3. Mean and (high, low) ranges of $\log_{10} K_d$ calculated for three ion exchanging minerals and three radionuclides.

RN	$\log_{10} K_d$ (mL/g)		
	Smectite	**Illite**	**Zeolite**
Ca(II)	2.9 (2.9, 2.9)	2.2 (2.2, 2.2)	3.4 (3.4, 3.4)
Cs(I)	2.0 (2.0, 1.5)	4.6 (4.6, 3.7)	3.5 (3.5, 2.9)
Sr(II)	2.9 (2.9, 2.9)	2.2 (2.2, 2.2)	3.5 (3.5, 3.4)

Table B.4. Mean and (high, low) ranges of $\log_{10} K_d$ calculated for surface complexation reacting minerals.

RN	$\log_{10} K_d$ (mL/g)			
	Goethite	**Smectite**	**Calcite**	**Hematite**
Ca(II)	–	–	1.7 (1.7, 1.7)	–
Cs(I)	–	–	–	–
Sr(II)	1.9 (2.5, 1.4)	–	–0.1 (0.9, –1.1)	0.6 (1.2, 0.1)
Am(III)	5.4 (6.2, 4.6)	4.7 (5.5, 4.1)	5.7 (6.7, 4.7)	4.1 (4.9, 3.3)
Eu(III)	5.5 (6.7, 4.3)	4.0 (5.1, 2.9)	5.6 (6.5, 4.6)	4.2 (5.4, 3.0)
Sm(III)	5.7 (6.9, 4.5)	4.2 (5.2, 3.1)	6.1 (7.0, 5.1)	4.4 (5.5, 3.2)
Np(V)	3.8 (4.7, 3.2)	1.1 (1.7, 0.7)	3.0 (4.0, 2.0)	2.5 (3.4, 1.9)
Pu(IV, V)	4.6 (5.6, 3.6)	2.0 (3.0, 1.0)	3.3 (4.2, 2.3)	3.3 (4.3, 2.3)
U(VI)	4.5 (5.4, 3.6)	1.2 (2.0, 0.6)	–0.7 (0.3, –1.7)	3.2 (4.0, 2.3)
Pu(IV, V)[a]	3.2 (4.2, 2.2)	0.8 (1.8, –0.2)	2.1 (3.1, 1.1)	1.9 (2.9, 0.9)

[a] K_d was modeled using an $f(O_2)$ of 0.2 in which Pu redox is dominated by the +6 state.

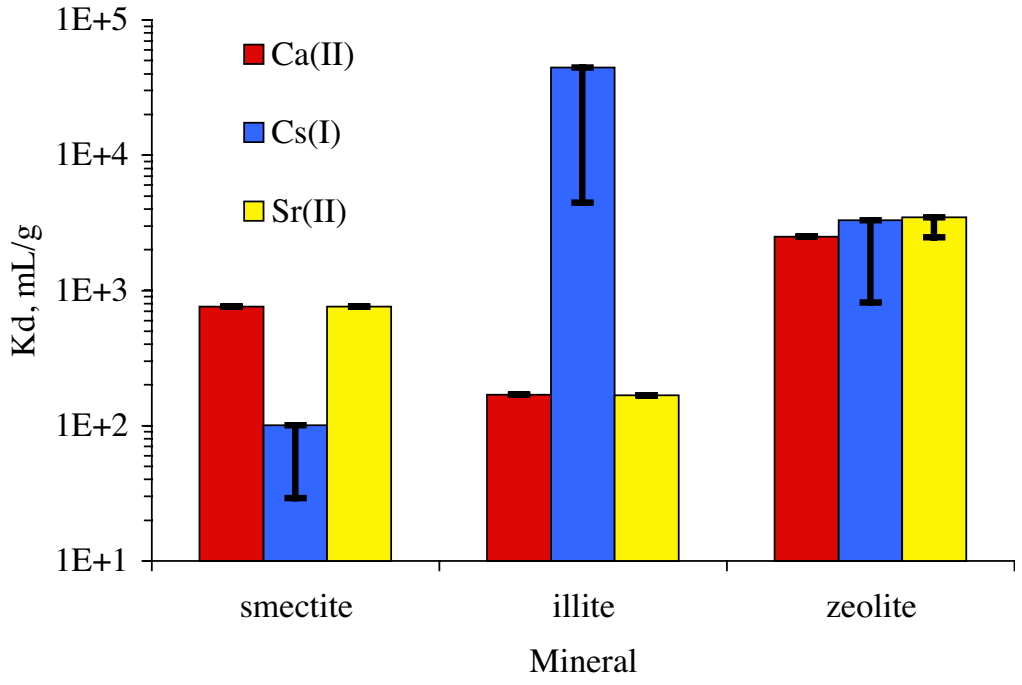

Figure B.1. K_d s calculated for three ion exchanging minerals and three radionuclides. Error bars are estimates of uncertainty.

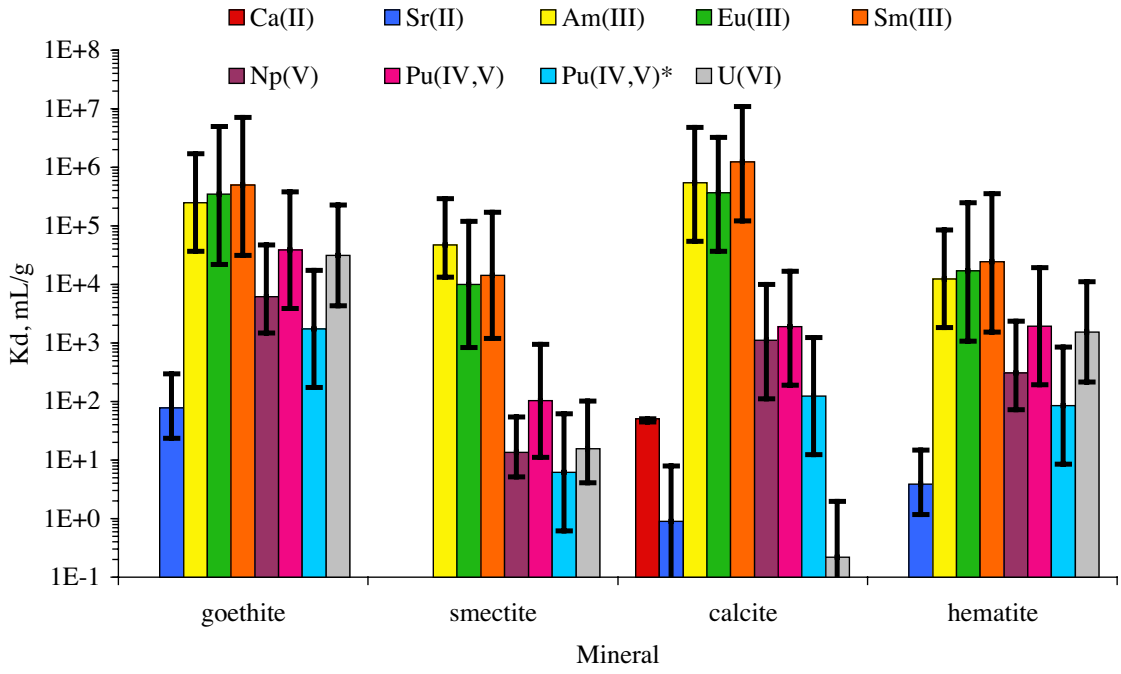

Figure B.2. K_d s calculated for surface complexing minerals. Error bars based on 2 standard deviations of surface complexation constants. [*K_d was modeled using an f(O_2) of 0.2 in which Pu redox is dominated by the +6 state.]

To calculate the effective or overall K_d for the Frenchman Flat alluvium described in Table B.1, the following equation is used:

$$K_d^i = \sum_m \frac{\phi_m \rho_m}{\rho_b} K_d^{i,m} \tag{B.1}$$

where K_d^i is the effective alluvium sorption constant for radionuclide i (mL/g), ϕ_m is the volume fraction of mineral m, ρ_m is the intrinsic density of mineral m, ρ_b is the bulk density of alluvium, and $K_d^{i,m}$ is the sorption constant (mL/g) for radionuclide i on mineral m. Table B.5 and Figures B.3 and B.4 present this data. Note that the "high" and "low" values in this case were calculated using Equation B.1 and the upper or lower limit values for all minerals in combination (i.e. the uncertainty was estimated simply as a linear combination of uncertainties in the single mineral $K_d^{i,m}$ data). As in the earlier figures, K_d s for Pu assuming a Pu(V) dominated and Pu(VI) dominated redox and retardation assuming a goethite-dominated and hematite-dominated alluvium are presented. Again, in the more oxic state, Pu is >1 order of magnitude less retarded. If the iron oxide reactive surface area is assumed to be equivalent to that of our "hematite alluvium" case, Np, Pu, and U retardation will be reduced by ~1 order of magnitude compared with the "goethite alluvium." Other radionuclides are less affected by iron oxide surface area because their retardation is controlled more by other minerals (see Figures B.1 and B.2).

It is instructive to compare the K_d^i values modeled here with the limited experimental data available for Frenchman Flat alluvium. Wolfsberg (1978) performed several sorption experiments and recommended K_d values for Sr, Cs, and Eu of 217±45, 7,000±1,600, and >20,000, respectively. The K_d values estimated here for Sr, Cs, and Eu using the model water composition and model mineralogy are 316 (316, 251) and 1000 (1000,158) for Sr and Cs, respectively (where values in parentheses represent an approximate uncertainty range). For Eu, K_d values using a goethite alluvium is 16,000 (200,000, 1,200) and, using a hematite alluvium is 7,900 (79,000, 790). The match between the modeled and experimental data is good, especially since "average" mineralogies and water chemistries were used in the predictions. A small set of U sorption experiments by Wolfsberg (1978) resulted in an average K_d of 29. For U, K_d values using the "goethite alluvium" case is 790 (6300,130) and, using the "hematite alluvium" case, is 50 (398,8). A reasonable match is made only when a "hematite-dominated" alluvium K_d is used. Remember that the "hematite-dominated" alluvium is based on the same reactions but a smaller reactive surface area. While this data is woefully inadequate to make any conclusions, it suggests that the K_d^i values based on the "hematite alluvium" case in Table B.5 will result in a more appropriate (or, at the very least more conservative) measure of retardation.

Table B.5. Mean and (high, low) ranges of effective $\log_{10} K_d^i$ for Frenchman Flat alluvium.

RN	$\log_{10} K_d^i$ (mL/g)	
	Goethite alluvium	Hematite alluvium
Ca(II)	2.4 (2.4, 2.4)	2.4 (2.4, 2.4)
Cs(I)	3.0 (3.0, 2.2)	3.0 (3.0, 2.1)
Sr(II)	2.5 (2.5, 2.4)	2.5 (2.5, 2.4)
Am(III)	4.3 (5.2, 3.5)	4.2 (5.1, 3.3)
Eu(III)	4.2 (5.3, 3.1)	3.9 (4.9, 2.9)
Sm(III)	4.6 (5.6, 3.5)	4.4 (5.3, 3.4)
Np(V)	2.3 (3.2, 1.6)	1.5 (2.4, 0.7)
Pu(IV, V)	3.0 (4.0, 2.0)	2.0 (3.0, 1.0)
U(VI)	2.9 (3.8, 2.1)	1.7 (2.6, 0.9)
Pu(IV, V)[a]	1.7 (2.7, 0.7)	0.8 (1.8, –0.2)

[a] K_d was modeled using an O_2(g) fugacity of 0.2 bars in which Pu redox is dominated by the +6 state.

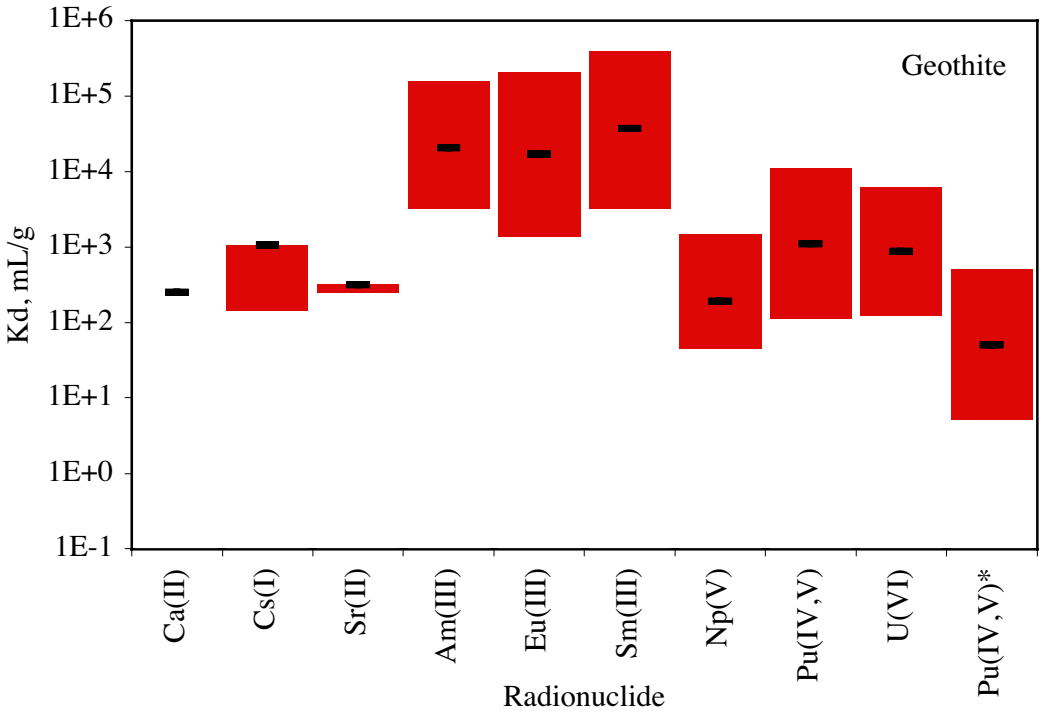

Figure B.3. Modeled K_d s for alluvium composition equivalent to that described in Tompson et al. (1999) and Table B.1. K_d s were estimated by assuming iron oxide is dominated to goethite. K_d range based on a composite uncertainty of all surface complexation and ion exchange constants. [*K_d was modeled using an O_2(g) fugacity of 0.2 bars in which Pu redox is dominated by the +6 state.]

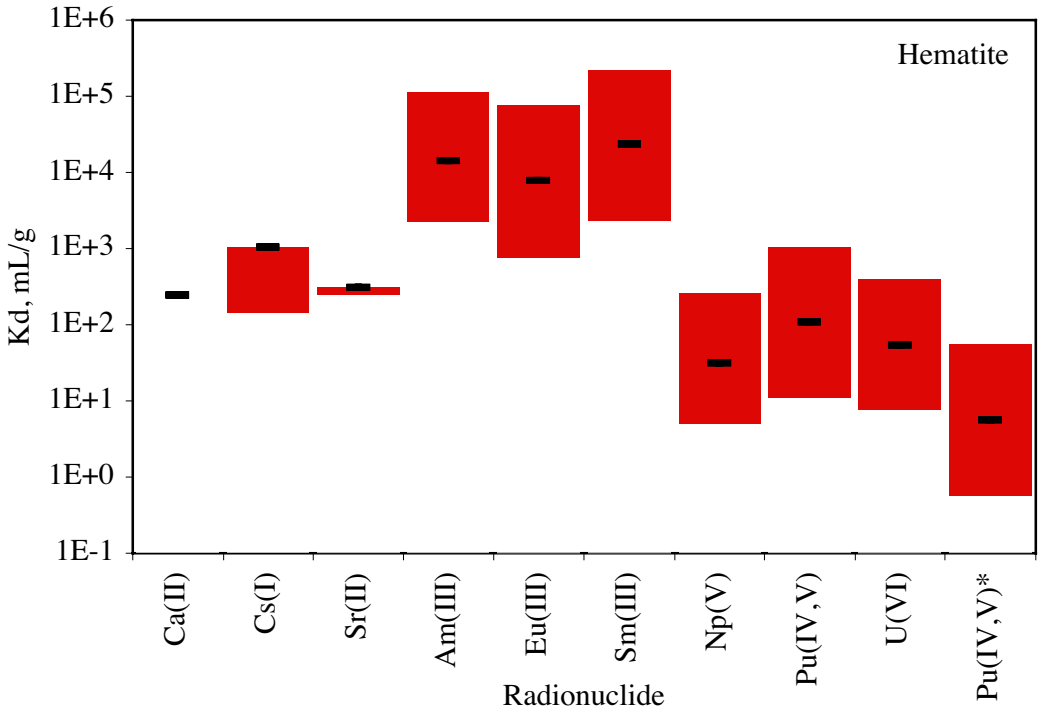

Figure B.4. Modeled K_d s for alluvium composition equivalent to that described in Tompson et al. (1999) and Table B.1. K_d s were estimated by assuming iron oxide is dominated to hematite. K_d range based on a composite uncertainty of all surface complexation and ion exchange constants. [*K_d was modeled using an O_2(g) fugacity of 0.2 bars in which Pu redox is dominated by the +6 state.]

Appendix C: Simplified Glass Dissolution Model

The release of elements from a volume of fractured or porous glass into an aqueous interstitial fluid is often described by a transition state theory-type rate law of the form

$$\frac{dN_i}{dt} = \nu_i A k \prod_j a_j^{p_j} \left(1 - \frac{Q}{K}\right) \tag{C.1}$$

where N_i is the number of moles of component i released, A is the reactive surface area of the glass (m^2) in the volume adjacent to the fluid, v_i is the stoichiometric coefficient for the element i in the glass (moles of element i per mole of glass), k is the rate coefficient (moles/m^2-sec), Π is the product function of catalytic or inhibitive species, and Q and K are the activity product and solubility product for the glass dissolution reaction (Aagaard and Helgeson, 1982) . If Equation C.1 is normalized by the bulk volume of glass considered (and the glass can be treated as a porous medium), we obtain the alternative form

$$\phi_g \frac{dc_i}{dt} = \nu_i r_g = \nu_i A_s k \prod_j a_j^{p_j} \left(1 - \frac{Q}{K}\right) \tag{C.2}$$

where c_i is the aqueous concentration of radionuclide i in the interstices (mol/ m^3-liquid), ϕ_g is the melt glass porosity, and $A_s = A / V_{gb}$ is the **specific** reactive surface area of the glass per unit bulk volume (m^2-glass /m^3-bulk volume) of the porous medium. The specific surface area can also be expressed as $A_s = A_s^m \rho_{gb}$ where A_s^m is the **specific** reactive surface area of the glass per unit mass (m^2-glass /g-glass), the more commonly measured quantity, and ρ_{gb} is the bulk density of the glass.

For the case of melt glass dissolution, the product term (Π_j) accounts for the effect of pH on the dissolution rate, where a_j is the activity of H^+ and p_j corresponds to the slope of the logarithm of the rate vs. pH. The quantity (1-Q/K) is the saturation or affinity term and provides for the slow-down in dissolution rate due to saturation. Commonly, only the effect of dissolved silica (SiO_2) is included in the saturation term in modeling silicate glass dissolution (Bourcier, 1994).

The rate constant k and the pH dependence of the glass dissolution rate are fairly well known. However, the dependence of the glass dissolution rate on solution chemistry is a more complex matter and can be affected flow rates and secondary mineral precipitation. This potential variability is the source of great uncertainty, especially in models such as GOLDSIM which do not directly address these interactions.

Because fluid chemistry and secondary mineral precipitation are neglected in GOLDSIM, a simplified rate law was developed for GOLDSIM that is equal to the product of two operationally

constant terms, namely, a modified rate constant, k^{mod}, and an approximately constant reactive surface area, A_s. Under these conditions, Equation C.2 simplifies to

$$\phi_g \frac{dc_i}{dt} = \nu_i r_g \approx \nu_i A_s k^{\mathrm{mod}}. \tag{C.3}$$

Some ranges and limits of k^{mod} are given below in order to capture elements of the potential variability introduced by chemical interactions in the melt glass. The intrinsic values of melt glass area, mass, and volume will change slowly over the course of dissolution. In this analysis, their magnitudes will be considered effectively fixed in order to not to change or otherwise affect the magnitude of the dissolution rate. For reference, the temperature dependence of glass dissolution can be expressed by an Arrhenius relationship as discussed in Section C.3, although temperature dependence **will not be** considered further here.

C.1 Modified Rate Constant

The modified rate constant, k^{mod}, is the product of the intrinsic rate constant (k), its pH dependence (in the product term, Π_j) and the saturation or affinity term (1-Q/K):

$$k^{\mathrm{mod}} = k \prod_j a_j^{p_j} \left(1 - \frac{Q}{K}\right). \tag{C.4}$$

In practice, most researchers group the first two terms in this equation—the rate constant and its pH dependence—into a single parameter and plot this parameter as a function of pH. This allows the pH dependence of these two terms to be fit in terms of three linear equations representing the negatively sloped dependence at low pH, the pH independent regime at intermediate pH, and the positively sloped dependence at high pH.

The saturation term was evaluated under the assumption that silica in solution is held in equilibrium with β-cristobalite, a solid form of silica. This means that the value of Q will take on a fixed value (Tompson et al., 1999) and that the saturation term as a whole will be constant. Assuming that the temperature is 25°C and that amorphous silica saturation defines the value of K, the magnitude of the saturation term used for these simple calculations is 0.489.

We coupled the above data with assumptions regarding the evolution of the chemical environment during melt glass dissolution to estimate probable ranges and limiting values of melt glass dissolution. The current best-guess "moderate" rate constant of glass dissolution[11] of

$$k^{\mathrm{mod}} \cong 5.1 \times 10^{-12} \text{ mol-glass/m}^2\text{-sec} = 5.1 \times 10^{-10} \text{ g-glass/m}^2\text{-sec} \tag{C.5a}$$

[11] A mole refers to a mole of glass, which is defined as 100 grams of glass.

at 25°C is obtained assuming that the ambient pH (8) and composition of groundwater is generally maintained during glass dissolution. The rate constant changes to

$$k^{\text{mod}} \cong 2.5 \times 10^{-12} \text{ mol-glass/m}^2\text{-sec} = 2.5 \times 10^{-10} \text{ g-glass/m}^2\text{-sec} \quad \text{(C.5b)}$$

and

$$k^{\text{mod}} \cong 1.4 \times 10^{-11} \text{ mol-glass/m}^2\text{-sec} = 1.4 \times 10^{-9} \text{ g-glass/m}^2\text{-sec} \quad \text{(C.5c)}$$

if the pH decreases or increases by an order of magnitude, respectively. The range of 2.2×10^{-12} and 2×10^{-11} mol/m^2-sec is our current best guess of the likely range of modified dissolution rate constants (k^{mod}) under near-ambient conditions. However, there is a very limited chance that the rate could increase to 4.5×10^{-10} mol/m^2-sec if the pH rises to about 12. There is also a chance, more likely than the high pH rate constant, that the rate will slow down to near-saturation values of 2.4×10^{-14} mol/m^2-sec. Rate constants are not expected to be lower than 2.4×10^{-14} mol/m^2-sec or higher than 4.5×10^{-10} mol/m^2-sec.

C.2 Reactive Surface Area

Determining the reactive surface area of melt glass is a problem that is complicated by the heterogeneous nature of the glass and, to a lesser degree, by the difficulty in understanding how changes in area occur over time as a function of progressive glass dissolution.

Photos of nuclear melt glass taken from post-test exploratory tunnels at Rainier Mesa (e.g., Wadman and Richards, 1961) show that the glassy zone is a breccia of rhyolite blocks, introduced during cavity collapse, incorporated into a melt glass horizon that is variably cracked and vesiculated (full of gas bubbles and having a texture similar to pumice). The relative proportions of massive, fractured, and vesicular glass are unknown, and their distributions in space are probably chaotic. In addition, when glasses cool from the outside, thermal gradients normal to the cooling surface produce differential thermal contraction that causes cracking. Reactions between the melt glass and water will give rise to hydrous alteration products that have a tendency to decrease permeability. Long term dissolution will also modify the reactive surface area of the glass.

To begin to address these issues, Bourcier et al. (2001) measured the specific reactive surface areas of intact rhyolite glass cores with a variety of textures. The rhyolites are used as analogues for melt glass. The average surface area measured was

$$A_s^m \sim 0.0026 \text{ m}^2\text{/g-glass} \quad \text{(C.6a)}$$

with a standard deviation of 0.0019 m^2/g. Bourcier et al. (2001) recommended that a range of

$$A_s^m \sim 0.001 \text{ to } 0.01 \text{ m}^2\text{/g-glass} \quad \text{(C.6b)}$$

be used for nuclear melt glass reactive surface area. This range was representative of glasses with a wide range of permeabilities and porosities. However, these samples probably had higher surface areas in general than melt glasses because melt glasses contain zones of massive glass in addition to the zones of brecciated and vesicular glass. The reactive surface area of massive glass could not be measured because it is impermeable. Water will contact only fractured surfaces in massive glass.

The reactive surface areas of fractured, man-made glass cylinders reported by Baxter (1983) are on the order of $A_s^m \sim 0.00005$ m^2/g, which is much lower than our measured reactive surface areas for vesicular and brecciated natural glass samples. Baxter's measurements were made on glass logs two feet in diameter and ten feet in length. The logs fracture during cooling due to thermal gradients, and dissolution in the reactive surface area test was localized along these fractures.

In recognition of the limited surface area of massive glass, the lower value of $A_s^m \sim 0.001$ m^2/g recommended by Bourcier et al. (2001) is being used in the CHESHIRE HST calculations at LLNL. However, the higher surface area of $A_s^m \sim 0.01$ m^2/g is being used in sensitivity calculations. Considerable uncertainty still exists regarding the spatial heterogeneity of reactive surface area owing to a lack of knowledge of in-situ conditions and of discrete flow paths in the melt glass zone.

Thus, we recommend fixed[12] values of A_s^m in the range 0.001 to 0.01 m^2/g-glass be used in GOLDSIM sensitivity studies. In addition, we will assume, for simplicity, that the overall rate of dissolution will be small enough so that changes in intrinsic area, volume, and mass of the melt glass (A, V_g, and M_g) will not be needed in the simplified source term calculations. This would imply that the derived values of A_s^m, A_s, and ρ_b will remain effectively constant. Additional studies related to the overall viability of this assumption are underway.

C.3 Temperature Dependence of Dissolution Rate

The rate constants (k) for glass dissolution vary with temperature according to the Arrhenius equation using an activation energy (Ea) of 20 kcal/mol:

$$\ln\left(\frac{k_2}{k_1}\right) = \frac{E_a}{R} \cdot \frac{T_2 - T_1}{T_2 T_1} \tag{C.7}$$

This expression will not be needed in the current analysis because the temperature is assumed fixed at 25°C for all time.

[12] By "fixed," we mean "constant" for the duration of a simulation. Different values may be used in different simulations, of course.

Appendix D: Some Errors in the CAMBRIC Simulations that Confused Interpretation

During the time this report was being prepared, two errors in the CAMBRIC simulations were uncovered that made comparison of the simulation results with the simplified source term predictions difficult. Both of these involve an incorrect or inconsistent (or both) specification of the melt glass inventories of Cs, Eu, Pu, and Am in the simulations.

D.1 First Error

In the first error, the radiologic melt glass inventory of Am, and to a smaller extent, those of Pu, Eu, and Cs, were specified incorrectly in the model, even though they can be readily calculated from the inventory and partitioning information in Tables 1 and 5 of the simulation report (Tompson et al., 1999, or "TBP"). Although the correct "target" inventories for the melt glass are included in Table 9 (p. 35), they are ultimately specified in the model via the stoichiometric coefficients (ν) that appear in Equation 4 of the report (p. 47). In the case of Cs, Eu, and Am, these were calculated incorrectly because of an error in computing the "Weight % Oxide" information in column 5 of Table 9 (p. 35) of the report. Here the stoichiometric factor of 2 between the moles of the element and moles of the oxide was not accounted for in the calculation and the "factor of two" error was propagated into Column 7 of Table 9 and then into Column 2 of Table 8. In the case of Eu and Cs, the errors were diluted by the fact that natural abundance of these elements was incorporated into the calculation[13] from Column 6 of Table 9. The end result was that the elemental compositions of these radionuclides, reported as moles per 100 grams of glass in Column 7 of Table 8 and later inserted into Equation 4[14], were incorrect. In the case of Pu, an error was created because of an incorrect specification of its molecular weight. Corrected versions of Tables 8 and 9 and Equation 4 of TBP are presented below in Tables D-1 to D-3.

For comparison, let us recompute the melt glass release flux for ^{241}Am based upon the "actual" (yet incorrect) inventory used in the simulation. Here, we insert the "as-simulated" value of ν for ^{241}Am found in Equation 4[15] of the report into Equation 3.11 to obtain:

$$J_g \approx \nu \cdot V_g \cdot A_s \cdot k^{\mathrm{mod}}$$

$$= (1.2 \times 10^{-6})(402\ \mathrm{m}^3)(118\ \mathrm{m}^2/\mathrm{m}^3)\ (10^{-13.36}\ \mathrm{mol/m^2\text{-}s})$$
$$= 2.48 \times 10^{-15}\ \mathrm{mol/s}$$
$$= 7.84 \times 10^{-8}\ \mathrm{mol/y} \qquad \text{(D.1)}$$

[13] See further discussion of this in Section D.2 below.

[14] Although reported per 100 g of glass in the last column of Table 8, they are subsequently scaled to moles per 10,000 g glass in Equation 4.

[15] We verified that the value in Equation 4 actually appeared in a revised database used in the simulations.

(compare with Equation 5.5b). Thus, we see in Figure 5.1 that although this "actual" glass flux changes the tail of the simplified release prediction, it does not seem to close the order-of-magnitude gap between the simplified release and the apparent glass flux in the corresponding simulation. Some additional discussion on this is included in Section 5.2.

Table D.1. Corrected version of Table 8 in the simulation report of Tompson et al. (1999). Unshaded rows: approximate composition of rhyolitic melt glass at CAMBRIC based upon data in Schwartz (1984). Shaded rows: approximate radioactive oxide composition in rhyolitic melt glass at CAMBRIC based upon inventory and partitioning data in Table D.2, molecular weights of the elements and oxides, and an estimate of 905 Mt of glass produced at CAMBRIC.

	Oxide			Element		
	Wt. %	**Mole %**	**Mol/100g**	**Wt. %**	**Mole %**	**Mol/100g**
O				49.6	64.2	3.1
SiO_2	75.9	82.5	1.26	35.5	26.1	1.3
Al_2O_3	13.7	8.8	0.13	7.3	5.6	0.27
Fe_2O_3	3.1	1.3	1.9×10^{-2}	2.2	0.8	3.9×10^{-2}
Na_2O	1.1	1.2	1.8×10^{-2}	0.9	0.8	3.7×10^{-2}
K_2O	2.9	2.0	3.0×10^{-2}	2.4	1.3	6.1×10^{-2}
P_2O_5	0.1	0.05	8.1×10^{-4}	0.05	0.03	1.6×10^{-3}
CaO	2.3	2.7	4.1×10^{-2}	1.6	0.8	4.1×10^{-2}
MgO	0.9	1.5	2.3×10^{-2}	0.6	0.5	2.3×10^{-2}
SrO	0.047	0.03	4.56×10^{-4}	4.0×10^{-2}	0.009	4.56×10^{-4}
PuO_2	3.7×10^{-4}	0.00	1.37×10^{-6}	3.27×10^{-4}	2.83×10^{-5}	1.37×10^{-6}
Am_2O_3	1.45×10^{-6}	0.00	2.72×10^{-9}	1.32×10^{-6}	1.13×10^{-7}	5.44×10^{-9}
Eu_2O_3	1.2×10^{-4}	0.00	3.29×10^{-7}	1.0×10^{-4}	1.36×10^{-5}	6.58×10^{-7}
Cs_2O	2.1×10^{-4}	–	7.52×10^{-7}	2.0×10^{-4}	3.11×10^{-5}	1.50×10^{-6}
Totals	100	100		100	100	

Table D.2. Corrected version of Table 9 in the simulation report of Tompson et al. (1999). Radionuclide abundances in melt glass at CAMBRIC based on 905 Mt of glass.

Element	Abundance (mol)	% in glass	Moles in glass	Wt% Oxide (rad)	Wt% Oxide (natural)	Wt% Oxide (total in model)	Oxide
^{90}Sr	3.4E-03	25	8.61E-04	9.9E-09	0.047	4.7E-02	SrO
^{137}Cs	1.1E-02	10	1.07E-03	1.7E-08	0.00021	2.1E-04	Cs_2O
^{155}Eu	8.5E-05	95	8.04E-05	1.6E-09	0.00012	1.2E-04	Eu_2O_3
^{239}Pu	1.3E+01	95	1.24E+01	3.7E-04	0	3.7E-04	PuO_2
^{241}Am	5.2E-02	95	4.93E-02	1.45E-06	0	1.45E-06	Am_2O_3

Table D.3. Corrected version of Equation 4 in the simulation report of Tompson et al. (1999). Coefficients represent ratio of moles of the element to moles of glass, where 1 mole of glass = 10,000 g of glass. Boldface indicates changed values.

$$\begin{aligned}\text{Melt glass} + 110.59\ H^+ \;=\; & 55.215\ H_2O \;+\; 0.965\ O_2(aq) \;+\; 126.24\ SiO_2(aq) \;+\; 26.888\ Al^{3+} \\ & +\; \mathbf{6.58 \times 10^{-5}\ Eu^{3+}} + 3.6861\ Na^+ \;+\; 6.06\ K^+ \;+\; \mathbf{1.367 \times 10^{-4}\ Pu^{4+}} \\ & +\; 2.27\ Mg^{2+} \;+\; \mathbf{1.504 \times 10^{-4}\ Cs^+} \;+\; \mathbf{4.56 \times 10^{-2}\ Sr^{2+}} \;+\; 3.86\ Fe^{2+} \\ & +\; 4.07\ Ca^{2+} \;+\; \mathbf{5.44 \times 10^{-7}\ Am^{3+}} \;+\; 40.16\ HPO_4^{2-}\end{aligned}$$

We have verified that these errors **were not** repeated in the recent classified Frenchman Flat simulations (Pawloski et al., 2000) nor in the recent CHESHIRE simulations (Pawloski et al., 2001).

For convenience, we recomputed the exchange volume release component based upon the dispersion formulation in Equation 3.4 above using a longitudinal macrodispersivity (α_L) of 17 m. With the exception of the slightly delayed speak arrival we see a more plausible exchange volume release in this result.

D.2 Second Error

The second error is related to the fact the both radiologic and naturally occurring amounts of Sr, Cs, and Eu were incorporated into the melt glass of the simulations[16] (e.g., Table 9, p. 35, TBP). However, they were, mistakenly, not incorporated into the initial exchange volume concentrations of these elements (e.g., Table 12, p. 59, TBP). Thus, the simulated integrated fluxes for Sr, Cs, and Eu in the report are inconsistent or incomplete as a result. As is, the flux results cannot be deconstructed, prior to decay correction, into their radiogenic and natural parts.

[16] Note that there is no naturally occurring Am in the simulations.

This would have allowed for a proper decay correction using different half-lives for the radiogenic and natural components to be applied, and a proper understanding of the radiogenic source term to be determined. Instead, the flux results were improperly decay-corrected using the half-life of the radiogenic component only, and over-represent the magnitude of the radiogenic source term flux.

Thus, trying to reproduce the simulated fluxes of Sr, Cs, and Eu using the simplified source term results would be somewhat of a haphazard process, as one would have to utilize the exact inventories used, albeit incorrect, and repeat the improperly applied decay correction. We chose not to do this for this report.

For reference, we have verified that **only** the radiogenic radionuclides were considered the recent classified Frenchman Flat and CHESHIRE simulations (Pawloski et al., 2000, 2001). No naturally occurring counterpart elements were built into the initial exchange volume or melt glass inventories in these simulations, so this problem was not repeated.

University of California
Lawrence Livermore National Laboratory
Technical Information Department
Livermore, CA 94551